

# Proximate integrability and exact revivals in staggered Rydberg ladders

Mainak Pal<sup>1,\*</sup> and Tista Banerjee<sup>1,†</sup>

<sup>1</sup>*School of Physical Sciences, Indian Association for the Cultivation of Science, Kolkata 700032, India*

Cold Rydberg atoms trapped in an array of optical tweezers can be manipulated using laser light. We investigate the fate of out-of-equilibrium quantum dynamics in a model of Rydberg atoms arranged in a square ladder geometry within the strong blockade regime, with a detuning profile staggered along the longer direction. As the staggering strength is tuned, the model exhibits a wide class of dynamical phenomena, ranging from quantum many-body scars, integrability-induced slow dynamics and approximate Krylov fractures. Furthermore, by leveraging the chiral nature of the spectrum, we design Floquet protocols which result in dynamical signatures reminiscent of discrete-time-crystalline order and exact Floquet-flat-bands.

*Introduction:* Rydberg atom quantum simulators [1] are a versatile platform to study fundamental aspects of quantum physics and have been extremely successful since their advent. These platforms have shaped our understanding of quantum phase transitions [2–6], topological phases of matter [7–9], out-of-equilibrium quantum dynamics [2, 10, 11], quantum state preparation [12, 13] and lattice gauge theories [14–18]. Such platforms offer a remarkable degree of tunability in terms of the geometry of the atomic arrangement as well as other system parameters controlled by external lasers, which make them an extremely promising platform to study a wide range of possible scenarios and novel phenomena.

In generic isolated interacting many-body quantum systems, where the total energy is the only conserved quantity, it is expected that an out-of-equilibrium initial state having sub-extensive energy fluctuations, relaxes quickly to a late-time thermal equilibrium which is entirely controlled by the initial energy density. Such a thermal equilibrium, attained under strict conditions of unitary quantum evolution, can be understood within the paradigm of the eigenstate thermalization hypothesis (ETH) [19–24]. However, in a landmark experiment [2], it was uncovered that under certain circumstances, a simple initial state evolving via an otherwise generic Hamiltonian may fail to thermalize in the above sense: i.e., certain initial states (for example, charge density wave states of various periods) undergo persistent revivals lasting several cycles throughout the life-time of the experiment, until which coherent unitary evolution could be maintained.

In subsequent theoretical studies [25, 26], these persistent many-body revivals were attributed to the presence of a tower of special eigenstates of the so-called PXP Hamiltonian [27] which is an idealized model representing the kinematical constraints induced in the strong Rydberg blockade regime [28–30] (i.e. no two atoms can be simultaneously be excited if they are within a certain radius) probed by the experiment. These special eigenstates were dubbed quantum many-body scars (QMBS) — a generalization of single-particle scars observed in quantum billiards [31] — which have (i) a considerable

overlap with these special initial states compared to most typical eigenstates and (ii) form an almost equidistant tower of states in energy. The combined effect of having these special features of the many-body eigenstates is the near perfect revivals observed in [2], and constitutes a weak form of ergodicity violation.

These developments were followed by a flurry of theoretical work exploring various models focusing on ergodicity violation, weak or strong, going beyond the well understood paradigm of integrable systems. This includes revisiting QMBS from different viewpoints [32–37], Hilbert space fragmentation [38–42] as well as exploring them on real quantum processors [43, 44]. Moreover, novel out-of-equilibrium phases such as a period two discrete-time-crystal (DTC) was also stabilized by leveraging the presence of QMBS [11].

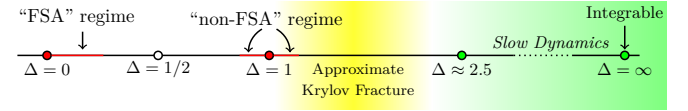


FIG. 1. Schematic illustration of the broad range of anomalous dynamical regimes hosted by the model (1) which can be accessed by adjusting a single parameter  $\Delta$

In this paper, we analyze the dynamical features of an idealized model of Rydberg atoms arranged in a square ladder geometry with a detuning profile staggered along the longer direction and blockade condition as depicted in Fig. 2. It was already pointed out in [45] that this model hosts quantum many-body scars (QMBS). However, we illustrate that for a large staggering strength, this model also exhibits slow dynamics and approximate Krylov fractures induced by approximate emergent integrability, as a consequence of the low-energy effective Hamiltonian being exactly integrable to second-order and higher order non-integrable terms contributing very weakly in this parameter regime. The particular form of the second-order effective Hamiltonian allows us to explicitly write down an extensive number of approximately conserved charges. These results imply that in this model one can access a broad range of non-equilibrium phenomena by

tuning a single adjustable parameter. Apart from such a rich structure in the quench dynamics, by leveraging the underlying chiral nature of the spectrum of the Hamiltonian, we have been able to design Floquet protocols leading to dynamical signatures reminiscent of discrete-time-crystalline (DTC) order [46–54] and exact Floquet flat bands, which are important in their own right due to their broader relevance in quantum control and quantum information processing.

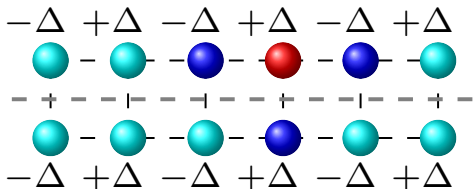


FIG. 2. A schematic representation of the 2-leg Rydberg (square) ladder setup with  $N = 2L = 12$  atoms and a staggered detuning profile ( $\Delta_{j,a} = (-1)^j \Delta$ ). The red (blue) sites depict the Rydberg excited (ground) states and illustrate the nature of the kinetic constraint in model (1)

Although we focus on the model (1), one may consider generalizations to higher-leg ladders and eventually the 2D square lattice. We have explored some of these generalizations in the Supplementary Material [55].

*Model:* Our focus will be on the nature of out-of-equilibrium quantum dynamics in the model governed by the Hamiltonian

$$\hat{H} = \sum_{j=1}^L \sum_{a=1}^2 \Omega \hat{P}_{j-1,a}^\downarrow \hat{P}_{j+1,a}^\downarrow \hat{P}_{j,\bar{a}}^\downarrow \hat{\sigma}_{j,a}^x - \Delta (-1)^j \hat{\sigma}_{j,a}^z \quad (1)$$

The model (1) is a non-perturbative generalization of the paradigmatic PXP chain [25, 26, 56], to the case of a 2-leg square ladder geometry with site-dependent detunings staggered along the longer direction. We denote by  $\hat{\sigma}_{j,a}^\alpha$ , spin- $\frac{1}{2}$  operators at site  $(j, a)$  where  $j = 1, 2, \dots, L, a = 1, 2, \alpha = x, y, z$ . The operators  $\hat{P}_{j,a}^\downarrow = (1 - \hat{\sigma}_{j,a}^z)/2$  are local projection operators onto the spin-down state at site  $(j, a)$ , and  $\hat{\sigma}_{j,\bar{a}}^\alpha = \hat{P}_{j-1,a}^\downarrow \hat{P}_{j+1,a}^\downarrow \hat{P}_{j,\bar{a}}^\downarrow \hat{\sigma}_{j,a}^\alpha$ . In the language of Rydberg atom quantum simulator platforms [2, 6, 57], the spin-down(up) states correspond to the Rydberg ground-(excited) states,  $(-1)^j \Delta$  are local detunings and  $2\Omega$  is the Rabi frequency. Henceforth, we fix  $\Omega = 1$ , and vary  $\Delta$  to access different dynamical regimes of (1). Such a generalization of the PXP chain, preserves properties such as spectral reflection symmetry and existence of an exponentially large number of zero modes protected by an index theorem, and can be attributed to the presence of two chirality operators  $\hat{C}_1 = \hat{T}_x \hat{C}$ ,  $\hat{C}_2 = \hat{T}_y \hat{T}_x \hat{C}$  anti-commuting with the Hamiltonian

$$\{\hat{C}_{1,2}, \hat{H}\} = 0 \quad (2)$$

Here  $\hat{T}_{x,y}$  denote the lattice-translation operators by one unit along the longer and the shorter directions respectively) and  $\hat{C} = \prod_{j=1}^L \prod_{a=1}^2 \hat{\sigma}_{j,a}^z$ . The property (2) implies that spectrum of  $\hat{H}$  has eigenpairs  $|\pm E\rangle$  i.e.  $\hat{H} |\pm E\rangle = \pm E |\pm E\rangle$  with  $|-E\rangle = \hat{C}_{1,2} |E\rangle$ . Furthermore, as the  $\hat{H}, \hat{C}_{1,2}$  have a spatial reflection symmetry, it follows from Ref. [58] that the spectrum of  $\hat{H}$  contains an exponentially large number (in system size  $N$ ) of exact mid-spectrum zero modes protected by an index theorem, for any value of  $\Delta$ .

Owing to such mathematical resemblance with the PXP chain, it is worth asking if the model (1) also exhibits non-equilibrium features, such as QMBS [2, 25, 26] or DTC order [11] observed in the PXP chain. This was partially explored in Ref. [45], where QMBS states were identified within the spectrum of  $\hat{H}$  for  $\Delta \sim 0, 1$ . Our goal in this paper is to present evidence of further anomalous behavior in the quench dynamics for a range of parameters, and to engineer Floquet protocols leading to dynamical signatures reminiscent of DTC order and exact Floquet-flat-bands.

*Quench Dynamics:* The schematic 1 illustrates the full non-equilibrium phase diagram of the model (1) vs  $\Delta$ . As  $\Delta$  changes from  $0 \rightarrow \infty$ , one encounters (i) two classes of QMBS — one describable by the forward scattering approximation (FSA) scheme ( $\Delta \sim 0$ ) and one not ( $\Delta \sim 1$ ), (ii) emergent integrability-induced slow dynamics and Krylov fractures ( $\Delta \gg 1$ ). We now focus on (ii) and refer the reader to [45] for a discussion of (i).

*Proximity to integrability:* In the limit  $\Delta \rightarrow \infty$ ,  $\hat{H}$  is completely integrable, i.e. all Fock states (in the  $\sigma^z$  basis) consistent with the local Hilbert space constraint, are eigenstates of  $\hat{H}$ . A perturbative construction of a low-energy effective Hamiltonian for large values of  $\Delta$ , via Schrieffer-Wolff (SW) transformation [59, 60] reveals that at second-order, the low-energy effective Hamiltonian still remains integrable. This is due to the fact that at second order, the effective Hamiltonian contains spin-flip processes (see Eq. (3)) which possess an extensive number of conserved charges, namely  $\hat{Z}_\pi = \sum_{j,a} (-1)^j \hat{\sigma}_{j,a}^z$ ,  $\hat{Q}_j = \hat{\sigma}_{j,1}^z \hat{\sigma}_{j,2}^z, \forall j = 1, 2, \dots, L$ . The existence of these conservation laws is understood by considering the action of  $\hat{H}_{\text{eff}}^{(2)}$  on the Fock states: the terms in the second summation of Eq. (3) essentially perform “blockaded spin-flips” i.e.  $|\dots \overset{\circ}{\sigma}_{j-1}^z \overset{\bullet}{\sigma}_j^z \overset{\circ}{\sigma}_{j+1}^z \dots\rangle \leftrightarrow |\dots \overset{\circ}{\sigma}_{j-1}^z \overset{\circ}{\sigma}_j^z \overset{\bullet}{\sigma}_{j+1}^z \dots\rangle$  where the “blockade” is due to the projectors  $\hat{P}^\downarrow$  at sites  $j \pm 1$  on both legs of the ladder. This leads to the realization of an effective two-site hopping of a Rydberg excitation  $\bullet$  between the two legs of the  $j^{\text{th}}$  rung, provided that this rung

is “blockaded” appropriately by Rydberg ground-states  $\circ$  at surrounding sites. Such processes have important consequences: (i) Fock states such as  $|\mathbb{Z}_2\rangle$  and  $|\text{vac}\rangle$  state, remain completely frozen under  $\hat{H}_{\text{eff}}^{(2)}$ , (ii) the expectation

$$\hat{H}_{\text{eff}}^{(2)} = -\frac{\Omega^2}{2\Delta} \sum_{j=1}^L (-1)^j \sum_{a=1}^2 \left[ \hat{\sigma}_{j,a}^z + \frac{1}{2} \hat{P}_{j-1,a}^\dagger \hat{P}_{j-1,\bar{a}}^\dagger \hat{P}_{j+1,a}^\dagger \hat{P}_{j+1,\bar{a}}^\dagger \hat{P}_{j,a}^\dagger \left( \hat{\sigma}_{j,a}^x \hat{\sigma}_{j,\bar{a}}^x + \hat{\sigma}_{j,a}^y \hat{\sigma}_{j,\bar{a}}^y \right) \right] \quad (3)$$

The third-order processes vanish exactly and integrability-breaking terms  $\sim \Omega^3/\Delta^4$  appear only at fourth-order. As a consequence, the short-range spectral correlations, as quantified by the distribution of the ratio ( $r_n$ ) of consecutive level spacings (see Ref. [61]), becomes Poissonian for  $\Delta \geq 2$  (see inset of Fig. 3). In contrast for  $\Delta \sim 1$ , the spectrum exhibits level repulsion (see inset of Fig. 3) akin to random matrices, although there is clear quantitative deviation from the Gaussian orthogonal ensemble (also see Supplementary for a comparison of exact and perturbative spectrum). This proximate integrability is not due to lattice symmetries of  $\hat{H}$ , which is evident from the main panel of Fig. 3 that represents the spectral analysis of the many-body energy levels of a modified Hamiltonian (Eq. (4)) having a weak on-site disorder on top of the perfectly staggered detuning profile.

$$\hat{H}_{\text{dis}} = \sum_{j=1}^L \sum_{a=1}^2 \Omega \hat{\sigma}_{j,a}^x - \sum_{j=1}^L \sum_{a=1}^2 (-1)^j (\Delta + \eta \mathcal{R}_{j,a}) \hat{\sigma}_{j,a}^z \quad (4)$$

Here,  $\mathcal{R}_{j,a} \sim \mathcal{U}[0,1]$ ,  $\forall j,a$  and  $\eta$  is the disorder strength. Fig. 3 shows that, although  $\hat{H}_{\text{dis}}$  does not have any lattice symmetries, the disorder-averaged mean consecutive level-spacing ratio  $\langle\langle r \rangle\rangle$  becomes close to  $2 \ln 2 - 1 \sim 0.386$  for  $\Delta \geq 2$ , and hence the observed Poissonian nature of the spectral statistics can be attributed to the extensive number of emergent conservation laws.

*Slow Dynamics and Equilibration to a generalized Gibbs ensemble (GGE):* Beyond  $\Delta = 2$ , as  $\Delta$  is further increased, the strength of integrability-breaking terms become increasingly negligible and the quasi-conservation of the charges  $\{\hat{Q}_j\}$  under  $\hat{H}$  becomes progressively accurate. As a consequence, certain initial states, exhibit exceptionally slow dynamics, as can be seen in Fig. 4 where the instantaneous expectation values of these operators under the full Hamiltonian i.e.  $\{\langle \hat{Q}_j(t) \rangle\}$  remain close to their initial values for very long times.

Fig. 5 shows that the expectation value of  $\hat{h}_{j,a} = \hat{\sigma}_{j,a}^x - \hat{\sigma}_{j,a}^z$  — a local observables of the model — under exact quantum evolution for  $\Delta \gg 1$ , starting from the state  $|\text{IP}\rangle = |\bullet^\circ\circ\circ\circ\circ\circ\rangle$ , still remains describable at late

values of  $\{\hat{Q}_j\}$  remain exactly conserved under evolution via  $\hat{H}_{\text{eff}}^{(2)}$  and (iii) the eigenstates of  $\hat{H}_{\text{eff}}^{(2)}$  can be labeled by the eigenvalues of  $\hat{Z}_\pi, \{Q_j\}$

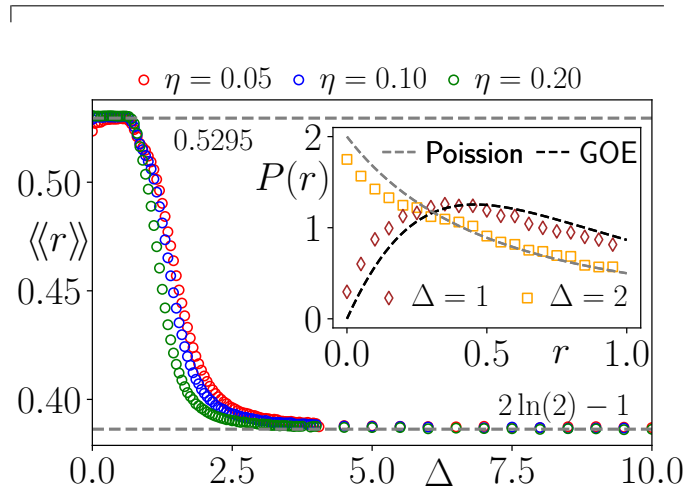


FIG. 3.  $P(r)$  vs  $r$  for (a)  $\Delta = 1$  and (b)  $\Delta = 2$  within the symmetry sector  $k_x = k_y = 1$  [55]. In both the figures black dashed line stands for gaussian orthogonal ensemble (GOE) statistics and gray dashed line stands for Poissonian statistics. (c) Disorder-averaged mean consecutive level-spacing ratio  $\langle\langle r \rangle\rangle$  vs  $\Delta$  for a system with  $N = 24$  sites averaged over 100 realizations for  $\eta = 0.05, 0.1, 0.2$ .

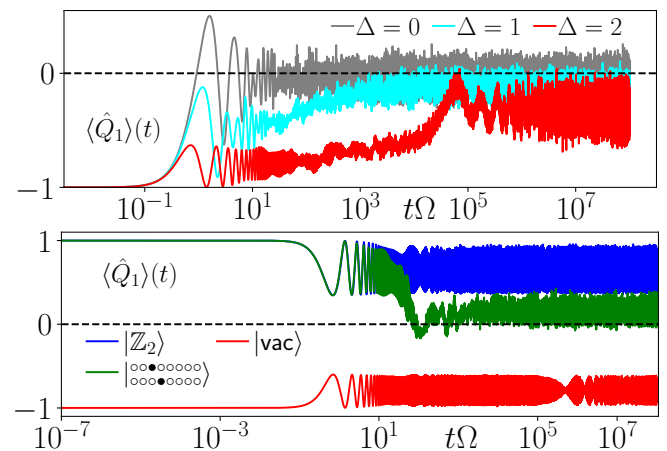


FIG. 4. Top: Slow dynamics of quasi-conserved charge  $\langle \hat{Q}_1 \rangle$ , under exact time-evolution for  $\Delta = 0, 1, 2$  starting from the initial state  $|\bullet^\circ\circ\circ\circ\circ\circ\rangle$ . Bottom: Slow dynamics from other initial states at  $\Delta = 2$ . For both panels  $N = 16$

times by a GGE determined from the quasi-conserved

charges  $\{Q_j\}$  [55]. For smaller values of  $\Delta$ , only the total energy is an exactly conserved quantity, and hence  $\langle \hat{h}_{j,a} \rangle(t)$  relaxes to a GE at the appropriate temperature.

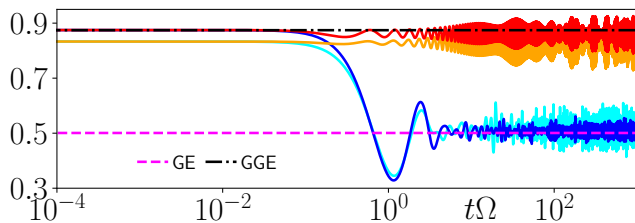


FIG. 5. Equilibration to GE and GGE: Relaxation of  $\langle \hat{h}_{1,1} \rangle(t)$ , starting from the  $|1P\rangle$  state. The dashed lines represent values of  $\langle \hat{h}_{1,1} \rangle(t)$  ( $\hat{h}_{1,1} = \hat{\sigma}_{1,1}^x - \hat{\sigma}_{1,1}^z$ ) predicted from GE (magenta) and GGE (black). The solid lines represent the results of the evolution under the full Hamiltonian (1) for (i)  $\Delta = 0$  with  $N = 16$  (blue),  $N = 12$  (cyan) and (ii)  $\Delta = 5$  with  $N = 16$  (red) and  $N = 12$  (orange)

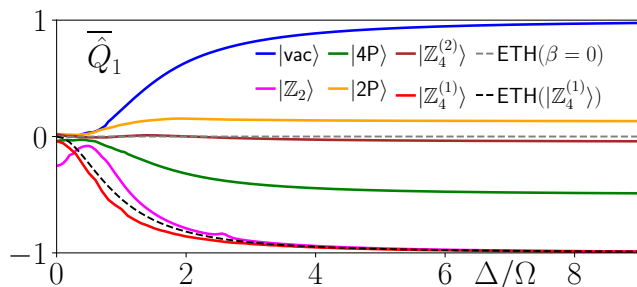


FIG. 6. Behavior of infinite-time average value  $\overline{\hat{Q}}_1$  and ETH values for  $\hat{Q}_1$  with  $\Delta$  for different initial states. See text for details.

Fig. 6 compares the infinite-time average and the ETH predicted values in GE of the quasi-conserved charge  $Q_1$  for a range of values of  $\Delta$  for different initial states:  $|\text{vac}\rangle$  (blue open circles),  $|Z_2\rangle$  (magenta open circles),  $|4P\rangle \equiv |\bullet\bullet\bullet\bullet\bullet\bullet\rangle$  (green open circles),  $|2P\rangle \equiv |\bullet\bullet\bullet\bullet\bullet\bullet\rangle$  (orange open circles),  $|Z_4^{(2)}\rangle \equiv |\bullet\bullet\bullet\bullet\bullet\bullet\rangle$  (brown open circles) and  $|Z_4^{(1)}\rangle \equiv |\bullet\bullet\bullet\bullet\bullet\bullet\rangle$  (red open circles). For all the aforementioned initial states  $|\psi(0)\rangle$  (except  $|Z_4^{(1)}\rangle$ ) we have  $\langle \psi(0) | \hat{H} | \psi(0) \rangle = 0$ , which combined with the fact that the spectrum of (1) has a reflection symmetry at any  $\Delta \neq 0$ , implies that all of these states should relax to the infinite temperature ( $\beta = 0$ ) GE, if they were to reach a thermal equilibrium. The ETH value of the quasi-conserved charges (dashed gray line) for  $\beta = 0$  is very close to zero ( $= 1/\mathcal{D}_H$ ,  $\mathcal{D}_H$  being the Hilbert space dimension). For the state  $|Z_4^{(1)}\rangle$ , however,  $\langle Z_4^{(1)} | \hat{H} | Z_4^{(1)} \rangle = -L\Delta$  and hence, the ETH value for  $\hat{Q}_1$  for this state changes with  $\Delta$  as shown in Fig. 6 (black dashed line), while the infinite-time average values are given as open red circles. This figure illustrates that the infinite-time average value of the quasi-conserved

charges, starting from the initial states with zero energy density, begin to drift away from the expected ETH value as  $\Delta$  is increased from zero and signals a form of ETH violation. For other states the ETH and the infinite-time average value coincide, implying that these states do not violate ETH.

For special initial states, the growth of correlations is extremely anisotropic and this is evident from Fig. 7 which shows the time-evolution of mutual information between two horizontally ( $I_{1,2}$ ) and vertically placed sites ( $I_{1,L_x}$ ) for the  $|1P\rangle$  state at  $\Delta = 4$  and  $N = 16$ . While for the horizontal bond the mutual information remains close to zero, for the vertical bond we observe large amplitude ( $\sim 2 \log 2$ ) oscillations and such contrasting behaviors along the two different directions of the lattice are traced back to the effective flip-flops  $|\bullet\circ\bullet\circ\bullet\circ\rangle \leftrightarrow |\circ\bullet\circ\bullet\circ\bullet\rangle$  happening at  $\Delta \geq 2$ . Such slow dynamics, along with the existence of simple local quasi-conserved charges  $\{q_j\}$  could in principle, be utilized to store  $L/2$  “classical” bits of information on a ladder of  $N = 2L$  sites [55].

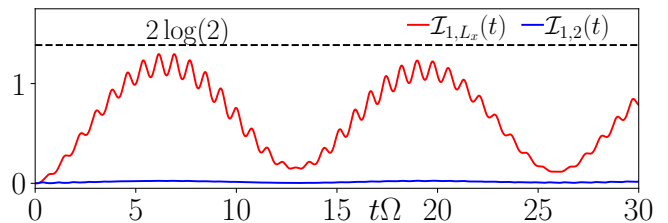


FIG. 7. Exact time-evolution of mutual information along horizontally (blue solid line) and vertically (red solid line) placed nearest neighbour sites for the initial state  $|1P\rangle$  at  $\Delta = 4$  with  $N = 20$  sites. See text for details.

The presence of quasi-conserved local charges  $\{q_j\}$  also influence the behavior of bi-partite von Neumann entanglement entropies ( $S_{\text{ent}}^{\text{vN}}(|E\rangle)$ ) of the eigenstates  $|E\rangle$  of  $\hat{H}$ . Fig. 8 shows a broad distribution for the values of  $S_{\text{ent}}^{\text{vN}}(|E\rangle)$  (even near  $E = 0$ ), and implies an approximate Krylov fracture for  $\Delta \sim 2$ . A analytical construction of all eigenstates of  $\hat{H}_{\text{eff}}^{(2)}$  [55] allows us to classify these eigenstates using the number of Bell-pairs the two rungs of the lattice share. The estimates  $S_{\text{ent}}^{\text{vN}}(|E\rangle)$  for two such classes of eigenstates are designated as dashed gray lines in the inset of Fig. 8(b) at values  $\log 2$  and  $2 \log 2$  which correspond to one and two shared Bell pairs respectively.

We note here that the model described by Eq. (1) is strictly integrable only when  $\Delta = \infty$ . However, even for large values of  $\Delta$  (i.e.  $\sim 2$ ), starting from any initial state, the system in the thermodynamic limit will eventually relax to the GE with the effective inverse temperature  $\beta$  is set by the initial energy density. To understand the onset of thermalization and the finite size effects, in the Supplementary Material we present the scaling behavior of the regularized adiabatic gauge potential (AGP) for different system sizes  $N$

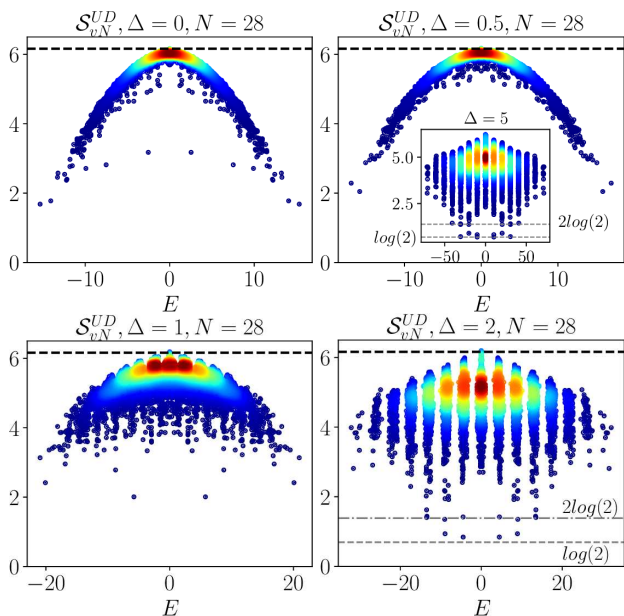


FIG. 8. Bipartite von Neumann entanglement entropy of all many-body eigenstates of  $\hat{H}$  with respect to UD partition for (a)  $\Delta = 0$ , (b)  $\Delta = 0.5$  (inset  $\Delta = 5$ ), (c)  $\Delta/\Omega = 1$  and (d)  $\Delta/\Omega = 2$  respectively for  $N = 28$  sites while the solid dashed black line denotes the corresponding Page value in the  $k_x = k_y = 0$  symmetry sector. The gray dashed/dotted lines indicates the estimates from the analytical construction of the eigenstates of  $\hat{H}_{\text{eff}}^{(2)}$  for states having one and two Bell pairs respectively [55].

and different values of  $\Delta$  [55], which has been used earlier as a sensitive indicator for quantum chaos [62]. Our results indicate that the model Eq. (1) is overall, quantum chaotic, even if various forms of ergodicity breaking behavior exist for finite-size systems at finite times for specific initial states. Furthermore, In the Supplementary Material [55] we also illustrate the stability of the emergent quasi-conservation laws against environmental loss channels such as spontaneous emission and dephasing.

*Floquet engineering exact revivals:* It is known that by leveraging the chirality operator associated with the PXP model (on any bi-partite lattice), it is possible to design Floquet protocols leading to dynamical signatures reminiscent of DTC order which are stabilized by QMBS [11]. Although, under the successive action of the Floquet-unitary  $\hat{U}_F^{(0)}(\tau) = \hat{C} e^{-i\tau\hat{H}}$  for model (1) also leads to period-2 exact sub-harmonic revivals starting from any initial state when  $\Delta = 0$ , this is not the case when  $\Delta \neq 0$  because  $\{\hat{H}_{\Delta \neq 0}, \hat{C}\} \neq 0$ . In this case, utilizing  $\hat{C}_1$  (or equivalently  $\hat{C}_2$ ), which are the chirality operators for our model in general when  $\Delta \neq 0$ , it is possible to generate two new classes of Floquet protocols, allowing us to realize exact revivals at any  $\Delta$ .

*Protocol-1, Subharmonic response:* Consider the fol-

lowing unitary operator, which is obtained by substituting  $\hat{C}_1$  (or  $\hat{C}_2$ ) for  $\hat{C}$  in  $\hat{U}_F^{(0)}(\tau)$ ,

$$\hat{U}_F^I(\tau) = \hat{C}_1 e^{-i\hat{H}\tau} \quad (5)$$

This protocol consists of unitary evolution via  $\hat{H}$  for a time  $\tau$  and the consequent action of  $\hat{C}_1$ , which itself is composed of a many-body  $\pi$ -pulse, followed by an (instantaneous) spatial translation of the atoms by one lattice-site along the direction of staggering, maintaining a periodic boundary condition. Successive action of the unitary  $\hat{U}_F^I(\tau)$  on any initial state of the system, defines for us a Floquet protocol, with  $\hat{U}_F^I(\tau)$  as the Floquet unitary having time period  $\tau$ . For such a protocol, we have  $\hat{U}_F^I(2m\tau) = \hat{T}_x^{2m}$  ( $m \geq 1$ ) [55], which implies that every Fock state returns to itself exactly after a number of cycles equal to its periodicity under  $\hat{T}_x$ . As a result of this delayed exact revivals, the interacting quantum many-body system described above exhibits a state-dependent sub-harmonic response (see Fig. 9), which is suggestive of DTC order [11, 54, 63]. An equivalent protocol can be constructed by replacing  $\hat{C}_1$  in  $\hat{U}_F^I$  by  $\hat{C}_2$ .

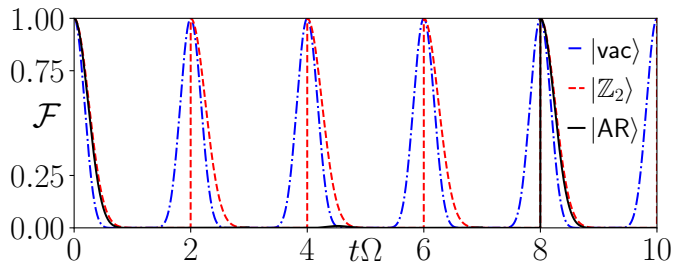


FIG. 9. Floquet micro-motion of *Protocol-1*: Return probability  $|\langle\psi(t)|\psi(0)\rangle|^2$  shown as a function of time starting from different initial states: (i)  $|\text{vac}\rangle$  (blue dashed), (ii)  $|\mathbb{Z}_2\rangle$  (red dashed) and (iii) a generic Fock state  $|\text{AR}\rangle \equiv |\bullet\circ\circ\circ\bullet\circ\circ\rangle$  (black solid) at  $\Delta = 0.5$  and  $N = 16$ .

*Protocol-2, Exact Floquet flat bands:* We now introduce a second class of Floquet protocol, which gives rise to exact revivals after each action of the unitary, starting from any initial state for any  $\Delta \neq 0$  and hence constitutes a different class of dynamical phenomena compared to *Protocol-1*. The one-cycle Floquet unitary for *Protocol-2* reads

$$\hat{U}_F^{\text{II}}(\tau) = \hat{C} e^{-i\hat{H}-\Delta_0\tau/2} \hat{C} e^{-i\hat{H}\Delta_0\tau/2} \quad (6)$$

Here,  $\hat{H}_{\pm\Delta_0}$  denotes the model Hamiltonian Eq. (1) with  $\Delta = \pm\Delta_0$ . Now, due to the identity  $\hat{C} e^{-i\hat{H}-\Delta_0\tau/2} \hat{C} = e^{+i\hat{H}+\Delta_0\tau/2}$  [55], we have  $\hat{U}_F^{\text{II}}(\tau) = \hat{1}$  which means *Protocol-2* gives rise to exact Floquet-flat-bands for any value of  $\Delta_0 \neq 0$  and that that under the action of  $\hat{U}_F^{\text{II}}(\tau)$ , any initial state exhibits exact

fidelity revivals with a time-period  $\tau$  (see Fig. 10).

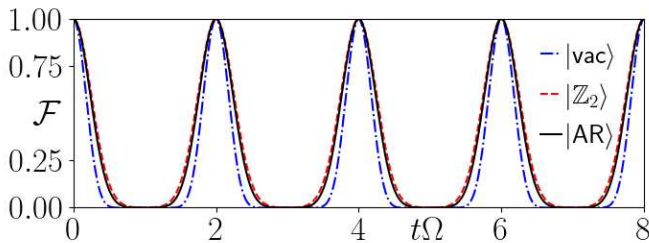


FIG. 10. Floquet micro-motion of *Protocol-2*: Return probability  $|\langle\psi(0)|\psi(t)\rangle|^2$  is shown as a function of time starting from different initial states (i)  $|\text{vac}\rangle$  (blue dashed line), (ii)  $|\mathbb{Z}_2\rangle$  (red dashed line) and (iii) a generic Fock state  $|\text{AR}\rangle = |\bullet\circ\circ\circ\bullet\circ\circ\circ\rangle$  (black dashed line) at  $\Delta_0 = 0.5$  and  $N = 16$ .

In Supplementary Material [55] we provide a basic analysis of the stability of the behaviors depicted in Fig. 9 and Fig. 10 against imperfections in the implementation of the many-body  $\pi$  pulse, and also against presence of small random disorder while implementing a staggered detuning profile.

*Conclusion and Outlook:* We demonstrated that in a model of Rydberg atoms in a ladder geometry with a staggered detuning profile along the longer direction, and with a specific Rydberg-blockading condition various forms of anomalous quantum dynamics are realized. Alongside the appearance of QMBS for  $\Delta \sim 0, 1$  [45] there exists a proximate integrable behavior for  $\Delta \geq 2$  whose quasi-conserved charges are exactly known. The existence of these quasi-conserved operators implies the presence of approximate Krylov fractures and integrability-induced slow dynamics. Furthermore we showed that by leveraging the chiral nature of the spectrum of the model, we can design Floquet protocols which allow us to realize dynamical behavior reminiscent of DTC order and exact Floquet flat bands.

Our analysis in this paper demonstrates that by engineering of the kinematic constraints as shown in Fig. 2, opens up a range of possibilities for exploring novel out-of-equilibrium phases and dynamical phenomena in real quantum hardware. We note here that by analyzing the more realistic long-range interacting model (see Supplementary Material), we have found that the specific form of kinetic constraint desired by our model may not be straightforwardly imposed, say by using atomic species with  $nS$ -type excited orbitals. Nonetheless since the model (1) exhibits a wide range of out-of-equilibrium phenomena, it is worth exploring alternate approaches to engineer such constraints. For example, using more sophisticated excited electronic orbitals as the Rydberg excited states, such as  $P$  or  $D$  orbitals may be useful, due to anisotropic interactions and magic distances [64]. Alter-

natively, one may also consider dressed Rydberg states, or mixtures of atomic species [65] in novel arrangements which can aid the engineering of such kinetic constraints in Rydberg atom quantum simulator platforms. In addition to the above, realization of such constrained systems may open up a gateway towards exploration of minimal models capable of mimicking interacting quantum field theories and lattice gauge theories present ubiquitously in particle physics apart from those already proposed theoretically and observed experiments in present day. [1, 14, 66].

*Acknowledgments:* The authors thank Arnab Sen, Immanuel Bloch, Peter Zoller, Klaus Mølmer, Vedika Khemani and Shovan Dutta for stimulating discussions and insightful comments. The authors would also like to acknowledge valuable discussions in two consecutive programs held at ICTS-TIFR – “A Hundred Years of Quantum Mechanics” (code: ICTS/qm100-2025/01) and “Quantum Trajectories” (code: ICTS/QuTr2025/01).

\* [intdydx@gmail.com](mailto:intdydx@gmail.com)

† [banerjeemou09@gmail.com](mailto:banerjeemou09@gmail.com)

- [1] H. Weimer, M. Müller, I. Lesanovsky, P. Zoller, and H. P. Büchler, A rydberg quantum simulator, *Nature Physics* **6**, 382 (2010).
- [2] H. Bernien, S. Schwartz, A. Keesling, H. Levine, A. Omran, H. Pichler, S. Choi, A. S. Zibrov, M. Endres, M. Greiner, V. Vuletić, and M. D. Lukin, Probing many-body dynamics on a 51-atom quantum simulator, *Nature* **551**, 579 (2017).
- [3] A. Keesling, A. Omran, H. Levine, H. Bernien, H. Pichler, S. Choi, R. Samajdar, S. Schwartz, P. Silvi, S. Sachdev, P. Zoller, M. Endres, M. Greiner, V. Vuletić, and M. D. Lukin, Quantum kibble-zurek mechanism and critical dynamics on a programmable rydberg simulator, *Nature* **568**, 207 (2019).
- [4] S. Ebadi, T. T. Wang, H. Levine, A. Keesling, G. Semeghini, A. Omran, D. Bluvstein, R. Samajdar, H. Pichler, W. W. Ho, S. Choi, S. Sachdev, M. Greiner, V. Vuletić, and M. D. Lukin, Quantum phases of matter on a 256-atom programmable quantum simulator, *Nature* **595**, 227 (2021).
- [5] M. Kalinowski, R. Samajdar, R. G. Melko, M. D. Lukin, S. Sachdev, and S. Choi, Bulk and boundary quantum phase transitions in a square rydberg atom array, *Phys. Rev. B* **105**, 174417 (2022).
- [6] A. Browaeys and T. Lahaye, Many-body physics with individually controlled rydberg atoms, *Nature Physics* **16**, 132 (2020).
- [7] S. K. Kanungo, J. D. Whalen, Y. Lu, M. Yuan, S. Dasgupta, F. B. Dunning, K. R. A. Hazzard, and T. C. Killian, Realizing topological edge states with rydberg-atom synthetic dimensions, *Nature Communications* **13**, 972 (2022).
- [8] S. de Léséleuc, V. Lienhard, P. Scholl, D. Barredo, S. Weber, N. Lang, H. P. Büchler, T. Lahaye, and A. Browaeys, Observation of a symmetry-protected topological phase of interacting bosons

- with rydberg atoms, *Science* **365**, 775 (2019), <https://www.science.org/doi/pdf/10.1126/science.aav9105>.
- [9] G. Semeghini, H. Levine, A. Keesling, S. Ebadi, T. T. Wang, D. Bluvstein, R. Verresen, H. Pichler, M. Kalinowski, R. Samajdar, A. Omran, S. Sachdev, A. Vishwanath, M. Greiner, V. Vuletić, and M. D. Lukin, Probing topological spin liquids on a programmable quantum simulator, *Science* **374**, 1242 (2021), <https://www.science.org/doi/pdf/10.1126/science.abi8794>.
- [10] D. Bluvstein, H. Levine, G. Semeghini, T. T. Wang, S. Ebadi, M. Kalinowski, A. Keesling, N. Maskara, H. Pichler, M. Greiner, V. Vuletić, and M. D. Lukin, A quantum processor based on coherent transport of entangled atom arrays, *Nature* **604**, 451 (2022).
- [11] N. Maskara, A. A. Michailidis, W. W. Ho, D. Bluvstein, S. Choi, M. D. Lukin, and M. Serbyn, Discrete time-crystalline order enabled by quantum many-body scars: Entanglement steering via periodic driving, *Phys. Rev. Lett.* **127**, 090602 (2021).
- [12] V. Crescimanna, J. Taylor, A. Z. Goldberg, and K. Heshami, Quantum control of rydberg atoms for mesoscopic quantum state and circuit preparation, *Phys. Rev. Appl.* **20**, 034019 (2023).
- [13] P. Scholl, A. L. Shaw, R. B.-S. Tsai, R. Finkelstein, J. Choi, and M. Endres, Erasure conversion in a high-fidelity rydberg quantum simulator, *Nature* **622**, 273 (2023).
- [14] F. M. Surace, P. P. Mazza, G. Giudici, A. Lerose, A. Gambassi, and M. Dalmonte, Lattice gauge theories and string dynamics in rydberg atom quantum simulators, *Phys. Rev. X* **10**, 021041 (2020).
- [15] D. González-Cuadra, M. Hamdan, T. V. Zache, B. Braverman, M. Kornjača, A. Lukin, S. H. Cantú, F. Liu, S.-T. Wang, A. Keesling, M. D. Lukin, P. Zoller, and A. Bylinskii, Observation of string breaking on a (2 + 1)d rydberg quantum simulator, *Nature* **642**, 321 (2025).
- [16] U. Borla, J. J. Osborne, S. Moroz, and J. C. Halimeh, String breaking in a 2+1d  $\mathbb{Z}_2$  lattice gauge theory (2025), [arXiv:2501.17929 \[quant-ph\]](https://arxiv.org/abs/2501.17929).
- [17] M. Meth, J. Zhang, J. F. Haase, C. Edmunds, L. Postler, A. J. Jena, A. Steiner, L. Dellantonio, R. Blatt, P. Zoller, T. Monz, P. Schindler, C. Muschik, and M. Ringbauer, Simulating two-dimensional lattice gauge theories on a qudit quantum computer, *Nature Physics* **21**, 570 (2025).
- [18] J. C. Halimeh and P. Hauke, Stabilizing gauge theories in quantum simulators: A brief review (2022), [arXiv:2204.13709 \[cond-mat.quant-gas\]](https://arxiv.org/abs/2204.13709).
- [19] J. M. Deutsch, Quantum statistical mechanics in a closed system, *Phys. Rev. A* **43**, 2046 (1991).
- [20] M. Srednicki, Chaos and quantum thermalization, *Phys. Rev. E* **50**, 888 (1994).
- [21] M. Srednicki, The approach to thermal equilibrium in quantized chaotic systems, *Journal of Physics A: Mathematical and General* **32**, 1163 (1999).
- [22] M. Rigol, V. Dunjko, and M. Olshanii, Thermalization and its mechanism for generic isolated quantum systems, *Nature* **452**, 854 (2008).
- [23] J. M. Deutsch, Eigenstate thermalization hypothesis, *Reports on Progress in Physics* **81**, 082001 (2018).
- [24] L. D'Alessio, Y. Kafri, A. Polkovnikov, and M. R. Anderson, From quantum chaos and eigenstate thermalization to statistical mechanics and thermodynamics, *Advances in Physics* **65**, 239 (2016), <https://doi.org/10.1080/00018732.2016.1198134>.
- [25] C. J. Turner, A. A. Michailidis, D. A. Abanin, M. Serbyn, and Z. Papić, Weak ergodicity breaking from quantum many-body scars, *Nature Physics* **14**, 745 (2018).
- [26] C. J. Turner, A. A. Michailidis, D. A. Abanin, M. Serbyn, and Z. Papić, Quantum scarred eigenstates in a rydberg atom chain: Entanglement, breakdown of thermalization, and stability to perturbations, *Phys. Rev. B* **98**, 155134 (2018).
- [27] P. Fendley, K. Sengupta, and S. Sachdev, Competing density-wave orders in a one-dimensional hard-boson model, *Phys. Rev. B* **69**, 075106 (2004).
- [28] D. Jaksch, J. I. Cirac, P. Zoller, S. L. Rolston, R. Côté, and M. D. Lukin, Fast quantum gates for neutral atoms, *Phys. Rev. Lett.* **85**, 2208 (2000).
- [29] D. Tong, S. M. Farooqi, J. Stanojevic, S. Krishnan, Y. P. Zhang, R. Côté, E. E. Eyler, and P. L. Gould, Local blockade of rydberg excitation in an ultracold gas, *Phys. Rev. Lett.* **93**, 063001 (2004).
- [30] M. D. Lukin, M. Fleischhauer, R. Cote, L. M. Duan, D. Jaksch, J. I. Cirac, and P. Zoller, Dipole blockade and quantum information processing in mesoscopic atomic ensembles, *Phys. Rev. Lett.* **87**, 037901 (2001).
- [31] E. J. Heller, Bound-state eigenfunctions of classically chaotic hamiltonian systems: Scars of periodic orbits, *Phys. Rev. Lett.* **53**, 1515 (1984).
- [32] C.-J. Lin and O. I. Motrunich, Exact quantum many-body scar states in the rydberg-blockaded atom chain, *Phys. Rev. Lett.* **122**, 173401 (2019).
- [33] C.-J. Lin, V. Calvera, and T. H. Hsieh, Quantum many-body scar states in two-dimensional rydberg atom arrays, *Phys. Rev. B* **101**, 220304 (2020).
- [34] S. Choi, C. J. Turner, H. Pichler, W. W. Ho, A. A. Michailidis, Z. Papić, M. Serbyn, M. D. Lukin, and D. A. Abanin, Emergent su(2) dynamics and perfect quantum many-body scars, *Phys. Rev. Lett.* **122**, 220603 (2019).
- [35] V. Khemani, C. R. Laumann, and A. Chandran, Signatures of integrability in the dynamics of rydberg-blockaded chains, *Phys. Rev. B* **99**, 161101 (2019).
- [36] C.-J. Lin, A. Chandran, and O. I. Motrunich, Slow thermalization of exact quantum many-body scar states under perturbations, *Phys. Rev. Res.* **2**, 033044 (2020).
- [37] C. J. Turner, J.-Y. Desaulles, K. Bull, and Z. Papić, Correspondence principle for many-body scars in ultracold rydberg atoms, *Phys. Rev. X* **11**, 021021 (2021).
- [38] P. Sala, T. Rakovszky, R. Verresen, M. Knap, and F. Pollmann, Ergodicity breaking arising from hilbert space fragmentation in dipole-conserving hamiltonians, *Phys. Rev. X* **10**, 011047 (2020).
- [39] V. Khemani, M. Hermele, and R. Nandkishore, Localization from hilbert space shattering: From theory to physical realizations, *Phys. Rev. B* **101**, 174204 (2020).
- [40] S. Moudgalya and O. I. Motrunich, Hilbert space fragmentation and commutant algebras, *Phys. Rev. X* **12**, 011050 (2022).
- [41] P. Brighi, M. Ljubotina, and M. Serbyn, Hilbert space fragmentation and slow dynamics in particle-conserving quantum East models, *SciPost Phys.* **15**, 093 (2023).
- [42] M. Ganguli, S. Aditya, and D. Sen, Aspects of Hilbert space fragmentation in the quantum East model: fragmentation, subspace-restricted quantum scars, and effects of density-density interactions (2024), [arXiv:2409.15943 \[cond-mat.stat-mech\]](https://arxiv.org/abs/2409.15943).
- [43] J.-Y. Desaulles, E. J. Gustafson, A. C. Y. Li, Z. Papić, and J. C. Halimeh, Robust finite-temperature many-

- body scarring on a quantum computer, *Phys. Rev. A* **110**, 042606 (2024).
- [44] E. J. Gustafson, A. C. Y. Li, A. Khan, J. Kim, D. M. Kurcuoglu, M. S. Alam, P. P. Orth, A. Rahmani, and T. Iadecola, Preparing quantum many-body scar states on quantum computers, *Quantum* **7**, 1171 (2023).
- [45] M. Pal, M. Sarkar, K. Sengupta, and A. Sen, Scar-induced imbalance in staggered rydberg ladders, *Phys. Rev. B* **111**, L161101 (2025).
- [46] D. V. Else, B. Bauer, and C. Nayak, Floquet time crystals, *Phys. Rev. Lett.* **117**, 090402 (2016).
- [47] N. Y. Yao, A. C. Potter, I.-D. Potirniche, and A. Vishwanath, Discrete time crystals: Rigidity, criticality, and realizations, *Phys. Rev. Lett.* **118**, 030401 (2017).
- [48] V. Khemani, A. Lazarides, R. Moessner, and S. L. Sondhi, Phase structure of driven quantum systems, *Phys. Rev. Lett.* **116**, 250401 (2016).
- [49] C. W. von Keyserlingk, V. Khemani, and S. L. Sondhi, Absolute stability and spatiotemporal long-range order in floquet systems, *Phys. Rev. B* **94**, 085112 (2016).
- [50] J. Zhang, P. W. Hess, A. Kyprianidis, P. Becker, A. Lee, J. Smith, G. Pagano, I.-D. Potirniche, A. C. Potter, A. Vishwanath, N. Y. Yao, and C. Monroe, Observation of a discrete time crystal, *Nature* **543**, 217 (2017).
- [51] S. Choi, J. Choi, R. Landig, G. Kucsko, H. Zhou, J. Isoya, F. Jelezko, S. Onoda, H. Sumiya, V. Khemani, C. von Keyserlingk, N. Y. Yao, E. Demler, and M. D. Lukin, Observation of discrete time-crystalline order in a disordered dipolar many-body system, *Nature* **543**, 221 (2017).
- [52] K. Sacha and J. Zakrzewski, Time crystals: a review, *Reports on Progress in Physics* **81**, 016401 (2017).
- [53] D. V. Else, C. Monroe, C. Nayak, and N. Y. Yao, Discrete time crystals, *Annual Review of Condensed Matter Physics* **11**, 467 (2020).
- [54] V. Khemani, R. Moessner, and S. L. Sondhi, *A brief history of time crystals* (2019), [arXiv:1910.10745 \[cond-mat.str-el\]](https://arxiv.org/abs/1910.10745).
- [55] See Supplementary Material for details or derivations.
- [56] S. Sachdev, K. Sengupta, and S. M. Girvin, Mott insulators in strong electric fields, *Phys. Rev. B* **66**, 075128 (2002).
- [57] D. Bluvstein, A. Omran, H. Levine, A. Keesling, G. Semeghini, S. Ebadi, T. T. Wang, A. A. Michailidis, N. Maskara, W. W. Ho, S. Choi, M. Serbyn, M. Greiner, V. Vuletić, and M. D. Lukin, Controlling quantum many-body dynamics in driven rydberg atom arrays, *Science* **371**, 1355 (2021), <https://www.science.org/doi/pdf/10.1126/science.abg2530>.
- [58] M. Schecter and T. Iadecola, Many-body spectral reflection symmetry and protected infinite-temperature degeneracy, *Phys. Rev. B* **98**, 035139 (2018).
- [59] J. R. Schrieffer and P. A. Wolff, Relation between the anderson and kondo hamiltonians, *Phys. Rev.* **149**, 491 (1966).
- [60] M. Sarkar, M. Pal, A. Sen, and K. Sengupta, Quantum order-by-disorder induced phase transition in Rydberg ladders with staggered detuning, *SciPost Phys.* **14**, 004 (2023).
- [61] V. Oganesyan and D. A. Huse, Localization of interacting fermions at high temperature, *Phys. Rev. B* **75**, 155111 (2007).
- [62] M. Pandey, P. W. Claeys, D. K. Campbell, A. Polkovnikov, and D. Sels, Adiabatic eigenstate deformations as a sensitive probe for quantum chaos, *Phys. Rev. X* **10**, 041017 (2020).
- [63] M. P. Zaletel, M. Lukin, C. Monroe, C. Nayak, F. Wilczek, and N. Y. Yao, Colloquium: Quantum and classical discrete time crystals, *Rev. Mod. Phys.* **95**, 031001 (2023).
- [64] B. Vermersch, A. W. Glaetzle, and P. Zoller, Magic distances in the blockade mechanism of rydberg  $p$  and  $d$  states, *Phys. Rev. A* **91**, 023411 (2015).
- [65] S. Anand, C. E. Bradley, R. White, V. Ramesh, K. Singh, and H. Bernien, A dual-species rydberg array, *Nature Physics* **20**, 1744 (2024).
- [66] J. I. Cirac, P. Maraner, and J. K. Pachos, Cold atom simulation of interacting relativistic quantum field theories, *Phys. Rev. Lett.* **105**, 190403 (2010).

# Supplemental Material for: “Proximate integrability and exact revivals in staggered Rydberg ladders”

Mainak Pal<sup>1,\*</sup> and Tista Banerjee<sup>1,†</sup>

<sup>1</sup>*School of Physical Sciences, Indian Association for the Cultivation of Science, Kolkata 700032, India*

(Dated: August 6, 2025)

## CONTENTS

S1. Symmetries of the Hamiltonian and Hilbert Space Dimensions	2
S2. Entanglement Measures	2
A. von Neuman Entanglement Entropy	2
B. Mutual Information	3
S3. Low-energy effective Hamiltonian for $\Delta \gg 1$	3
A. Full Spectrum of $\hat{H}_{\text{eff}}^{[2]}$	4
B. Eigenvalues of $\hat{H}$ , $\hat{H}_{\text{eff}}^{[2]}$ and $\hat{H}_{\text{eff}}^{[4]}$	5
C. Ensemble of relaxation: Gibbs vs Generalized Gibbs	5
D. Storing classical bits of information	6
S4. Derivation of the identity $\hat{C}e^{-i\hat{H}-\Delta_0\tau/2}\hat{C} = e^{+i\hat{H}+\Delta_0\tau/2}$	6
S5. Stability of exact revivals for an imperfect $\pi$ -pulse	7
S6. 3-leg ladder	8
A. Quantum many-body scars	8
B. Quasi-conserved charges and Slow Dynamics for $\Delta \gg 1$	8
S7. van der Waals interactions and validity of the first nearest neighbor Rydberg Blockade	9
A. 1D Rydberg Chain	10
B. 2-leg Rydberg Square Ladder	11
C. Two Dimensional Square Lattice	12
S8. Scaling of the norm of rescaled, regularized Adiabatic Gauge Potential	14
S9. Effects of environment	14
A. Stability of QMBS	15
1. Dephasing	15
2. Spontaneous emission	16
B. Stability of Approximate Emergent Conservation Laws	16
C. Individual Quantum Trajectories	17
References	18

---

\* [intdydx@gmail.com](mailto:intdydx@gmail.com)

† [banerjeemou09@gmail.com](mailto:banerjeemou09@gmail.com)

## S1. SYMMETRIES OF THE HAMILTONIAN AND HILBERT SPACE DIMENSIONS

In this section, we list the symmetries and the corresponding Hilbert space dimensions for the model studied in the main text. By inspection we note that for  $\Delta \neq 0$ , the Hamiltonian commutes with the operators  $\hat{T}_x^2$  and  $\hat{T}_y$ , where  $\hat{T}_x$  denotes translation by one lattice site along the longer direction and  $\hat{T}_y$  denotes reflection with respect to the same. We can construct a computational basis, in which the basis states are labeled by the eigenvalues of the symmetry operators  $\hat{T}_x^2$  and  $\hat{T}_y$  (see Ref. [S1] for a review on construction of symmetry reduced Hilbert spaces). For reference, in Table I, we list the Hilbert space dimensions of some chosen sectors of these symmetry operators.

$N$	No Symmetry	$k_x = 0$	$k_{x,y} = 0$	$k_x = 0, k_y = \pi$	$k_{x,y} = \pi$
4	7	7	5	2	0
8	35	21	12	9	8
12	199	71	36	35	32
16	1,155	301	156	145	144
20	6,727	1,351	676	675	672
24	39,203	6,581	3,308	3,273	3,264
28	228,487	32,647	16,324	16,323	16,320
32	1,331,715	166,621	83,388	83,283	83,232

TABLE I. Hilbert space dimensions of the model for system size  $N = 4 - 32$  without any symmetry and for some specific symmetry sectors (for  $\Delta \neq 0$ ) labeled by  $k_x$  and  $k_y$  (the eigenvalues of the symmetry operators  $\hat{T}_x^2$  and  $\hat{T}_y$  respectively).

We note that when  $\Delta = 0$ , the Hamiltonian  $\hat{H}$  commutes with the operators  $\hat{T}_x$ ,  $\hat{T}_y$  and  $\hat{P}_x$  and hence the model has additional lattice symmetries.

## S2. ENTANGLEMENT MEASURES

### A. von Neuman Entanglement Entropy

The bipartite von Neumann entanglement entropy [S2, S3] for any (pure) quantum state  $|\psi\rangle$ , for a given bi-partition  $\mathcal{X}, \mathcal{X}^c$  ( $\mathcal{X} \cup \mathcal{X}^c = \mathcal{E}$ , the entire system), is defined as,

$$S_{\text{ent}}^{\text{vN}}(\mathcal{X}) = -\text{Tr}_{\mathcal{X}}(\hat{\rho}_{\mathcal{X}} \log \hat{\rho}_{\mathcal{X}}) \quad (\text{S1})$$

where  $\rho_{\mathcal{X}} = \text{Tr}_{\mathcal{X}^c}(|\psi\rangle\langle\psi|)$  is the reduced density matrix (RDM) of sub-system  $\mathcal{X}$  with respect to its conjugate  $\mathcal{X}^c$ . For a ladder type geometry, two kinds of bi-partitions are natural (i) ‘‘LR’’ (short for left-right) partition and (ii) ‘‘UD’’ (short for up-down) partition. In the LR partition,  $\mathcal{X}$  is either taken to be left half or the right half of the ladder while for the UD partition,  $\mathcal{X}$  is either the upper leg or the lower leg of the ladder. For a kinetically constrained system, such as the PXP model or the model studied in the main text, the Hilbert space does not have a direct product structure: for any bi-partition  $\mathcal{X}, \mathcal{X}^c$  with  $\mathcal{X} \cup \mathcal{X}^c = \mathcal{E}$ , the full Hilbert space, say  $\mathcal{H}_{\mathcal{E}}$ , is not equivalent to the direct product of Hilbert spaces  $\mathcal{H}_{\mathcal{X}}$  and  $\mathcal{H}_{\mathcal{X}^c}$  i.e.,  $\mathcal{H}_{\mathcal{E}} \neq \mathcal{H}_{\mathcal{X}} \otimes \mathcal{H}_{\mathcal{X}^c}$  (both  $\mathcal{H}_{\mathcal{X}}$  and  $\mathcal{H}_{\mathcal{X}^c}$  are for open boundary conditions). In such a scenario, a quantum state  $|\psi\rangle \in \mathcal{H}_{\mathcal{E}}$ , can in principle be expressed in the product Hilbert space  $\mathcal{H}_{\mathcal{X}} \otimes \mathcal{H}_{\mathcal{X}^c}$  as

$$|\psi\rangle = \sum_{\alpha=1}^{\mathcal{D}_{\mathcal{X}}} \sum_{\beta=1}^{\mathcal{D}_{\mathcal{X}^c}} \psi_{\alpha,\beta}^{\mathcal{X},\mathcal{X}^c} |\Phi_{\alpha}^{\mathcal{X}}\rangle \otimes |\Phi_{\beta}^{\mathcal{X}^c}\rangle \quad (\text{S2})$$

where  $\{\psi_{\alpha,\beta}^{\mathcal{X},\mathcal{X}^c}\}$  are complex numbers describing the state,  $\{|\Phi_{\alpha}^{\mathcal{X}}\rangle\}, \{|\Phi_{\beta}^{\mathcal{X}^c}\rangle\}$  are Fock basis states for  $\mathcal{H}_{\mathcal{X}}$  and  $\mathcal{H}_{\mathcal{X}^c}$  respectively with Hilbert space dimensions  $\mathcal{D}_{\mathcal{X}}$  and  $\mathcal{D}_{\mathcal{X}^c}$ . The Hilbert space constraint is taken care of by setting  $\psi_{\alpha,\beta}^{\mathcal{X},\mathcal{X}^c} = 0$  if  $|\Phi_{\alpha}^{\mathcal{X}}\rangle \otimes |\Phi_{\beta}^{\mathcal{X}^c}\rangle \notin \mathcal{H}_{\mathcal{E}}$ . With the state  $|\psi\rangle$  expressed as in Eq. (S2), one can compute partial traces of the density matrix  $\hat{\rho} = |\psi\rangle\langle\psi|$  over sub-system  $\mathcal{X}^c$  to obtain the sub-system RDM  $\rho_{\mathcal{X}}$ , which can then be used to compute desired entanglement measures.

## B. Mutual Information

In the main text we also considered the evolution of mutual information between two sites. In general, the mutual information between any two subsystems,  $\mathcal{X}$  and  $\mathcal{Y}$  is defined as

$$I(\mathcal{X}, \mathcal{Y}) = S_{\text{ent}}^{\text{vN}}(\mathcal{X}) + S_{\text{ent}}^{\text{vN}}(\mathcal{Y}) - S_{\text{ent}}^{\text{vN}}(\mathcal{X} \cup \mathcal{Y}) \quad (\text{S3})$$

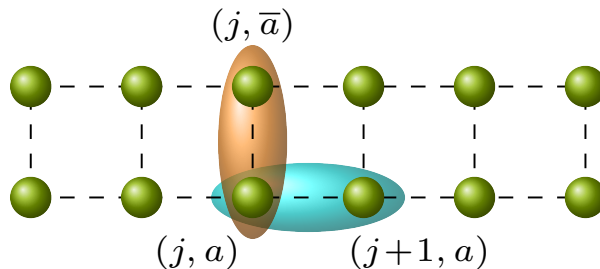


FIG. S1. Schematic illustration of the subsystems  $\mathcal{X}$ ,  $\mathcal{X}_c$  for the computation of mutual information between horizontally (cyan) and vertically (orange) placed nearest neighbour sites presented in the main text. Also see Eq. (S3) and text below it.

This quantity  $I(\mathcal{X}, \mathcal{Y})$  for any state, for any bi-partition  $\mathcal{X}, \mathcal{Y}$ , describes the total amount of correlation shared between  $\mathcal{X}$  and  $\mathcal{Y}$ , which includes both classical and quantum correlations [S4, S5]. From a quantum information point of view, the mutual information encodes the amount of information about the sub-system  $\mathcal{X}$  that can be obtained from the sub-system  $\mathcal{Y}$ . In this case, it is not necessary that  $\mathcal{X} \cup \mathcal{Y} = \mathcal{E}$ . For the specific results displayed in the main text, i.e. the mutual information of the horizontal bonds we take  $\mathcal{X} = \{(j, a)\}$ ,  $\mathcal{Y} = \{(j+1, a)\}$  and for vertical bonds we take  $\mathcal{X} = \{(j, a)\}$ ,  $\mathcal{Y} = \{(j, \bar{a})\}$  in Eq. (S3) with  $j = 1, a = 1$ .

### S3. LOW-ENERGY EFFECTIVE HAMILTONIAN FOR $\Delta \gg 1$

At  $\Delta = \infty$ , the spectrum of  $\hat{H}$  is known exactly: all computational basis states (i.e. Fock states in the  $\hat{\sigma}^z$  basis) are eigenstates of the Hamiltonian. To quantitatively study the effect of this integrable point for  $\mathcal{O}(1)$  values of  $\Delta$ , we construct a Schrieffer-Wolff (SW) transformation of the basis and make the effective Hamiltonian block diagonal in the eigenbasis of the diagonal part of the  $\hat{H}$ , i.e.  $\hat{H}_z = \Delta \sum_{j,a} (-1)^j \hat{\sigma}_{j,a}^z$ , up to first order in  $1/\Delta$ . The generator of this SW transformation  $i\hat{S}$  reads

$$i\hat{S} = -\frac{1}{2i\Delta} \sum_{j=1}^L \sum_{a=1}^2 (-1)^j \hat{\sigma}_{j,a}^y \quad (\text{S4})$$

The structure of the generator  $i\hat{S}$  implies

$$[i\hat{S}, \hat{H}_z] = -\hat{H}_x \quad (\text{S5})$$

In the above equation, the off-diagonal part of  $\hat{H}$  in the computational basis is denoted by  $\hat{H}_x$ , i.e.  $\hat{H}_x = \sum_{j,a} \hat{\sigma}_{j,a}^x$ . The effective low-energy Hamiltonian, in the appropriate rotated basis reads

$$\begin{aligned} \hat{H}_{\text{eff}} &= \hat{P}_{Z_\pi} \left( e^{i\hat{S}} \hat{H} e^{-i\hat{S}} \right) \hat{P}_{Z_\pi} \\ &= \hat{H}_{\text{eff}}^{(0)} + \hat{H}_{\text{eff}}^{(1)} + \hat{H}_{\text{eff}}^{(2)} + \hat{H}_{\text{eff}}^{(3)} + \dots \end{aligned} \quad (\text{S6})$$

Where

$$\begin{aligned}
\hat{H}_{\text{eff}}^{(0)} &= \hat{P}_{Z_\pi} \hat{H}_z \hat{P}_{Z_\pi} \\
\hat{H}_{\text{eff}}^{(1)} &= 0 \\
\hat{H}_{\text{eff}}^{(2)} &= \hat{P}_{Z_\pi} \left( \frac{1}{2!} [i\hat{S}, \hat{H}_x] \right) \hat{P}_{Z_\pi} \\
\hat{H}_{\text{eff}}^{(3)} &= \hat{P}_{Z_\pi} \left( \frac{1}{3!} [i\hat{S}, [i\hat{S}, \hat{H}_x]] \right) \hat{P}_{Z_\pi} = 0 \\
\hat{H}_{\text{eff}}^{(4)} &= \hat{P}_{Z_\pi} \left( \frac{1}{4!} [i\hat{S}, [i\hat{S}, [i\hat{S}, \hat{H}_x]]] \right) \hat{P}_{Z_\pi}
\end{aligned} \tag{S7}$$

In the above perturbation theory, all odd-order terms vanish and only even-order terms are non-trivial. By direct computation of the commutators, one arrives at the expression for  $\hat{H}_{\text{eff}}^{(2)}$

$$\hat{H}_{\text{eff}}^{(2)} = -\frac{1}{2\Delta} \sum_{j=1}^L \sum_{a=1}^2 (-1)^j \hat{\sigma}_{j,a}^z - \frac{1}{4\Delta} \sum_{j=1}^L \sum_{a=1}^2 (-1)^j \hat{P}_{j-1,a}^\downarrow \hat{P}_{j-1,\bar{a}}^\downarrow \hat{P}_{j+1,a}^\downarrow \hat{P}_{j+1,\bar{a}}^\downarrow \hat{P}_{j,a}^\downarrow \left( \hat{\sigma}_{j,a}^x \hat{\sigma}_{j,\bar{a}}^x + \hat{\sigma}_{j,a}^y \hat{\sigma}_{j,\bar{a}}^y \right) \tag{S8}$$

Already at second order, the effective Hamiltonian reveals the dominant physical processes taking place in the quench dynamics of the system. At this order, any Fock state which satisfies the blockading condition in Eq. (S8), undergoes Rabi oscillations induced via the  $XX + YY$  terms. This effective Hamiltonian also suggests that there are  $L$  number of emergent quasi-conserved charges for a system with  $2L$  sites. It is worth mentioning that, for a deeper understanding, it should be explored whether one can explicitly cast the effective Hamiltonian up to second order in a Bethe integrable form. For our model, the second-order effective Hamiltonian also exhibits slow dynamics due to existence of the following extensive number of conservation charges

$$\hat{Z}_\pi = \sum_{j=1}^L \sum_{a=1}^2 (-1)^j \hat{\sigma}_{j,a}^z \tag{S9}$$

$$\hat{Q}_j = \hat{\sigma}_{j,1}^z \hat{\sigma}_{j,2}^z \quad \forall j = 1, 2, \dots, L \tag{S10}$$

as shown in the main text. Considering the conservation of the total energy, we have  $L + 2$  number of constants of motion, which suggests that the effective Hamiltonian (up to second order) is integrable, and it is possible to write down explicitly the eigenvalues and eigenvectors of  $\hat{H}_{\text{eff}}^{[2]} = \hat{H}_{\text{eff}}^{(0)} + \hat{H}_{\text{eff}}^{(2)}$  in each charge sector labeled by the quantum numbers  $(z_\pi, q_1, q_2, \dots, q_L)$ . In the following section, we present an outline for the process of enumeration of all the eigenvectors and the eigenvalues of  $\hat{H}_{\text{eff}}^{[2]}$ .

### A. Full Spectrum of $\hat{H}_{\text{eff}}^{[2]}$

First, we note by inspection that the vacuum state  $|\text{vac}\rangle$  is annihilated by  $\hat{H}_{\text{eff}}^{[2]} = \hat{H}_{\text{eff}}^{(0)} + \hat{H}_{\text{eff}}^{(2)}$ , and hence is a zero-mode at second order. We now consider states with finite number of Rydberg excitations by forming singlets/triplets of the following form

$$|j, \pm\rangle_{1\text{P}} = \frac{1}{\sqrt{2}} \left( |\dots \overset{\bullet}{\circ}_j \dots\rangle \pm |\dots \overset{\circ}{\bullet}_j \dots\rangle \right) \tag{S11}$$

where for brevity of notation, the dots “...” within the  $|\rangle$  symbol, imply absence of Rydberg excitations. The states  $|j, \pm\rangle_{1\text{P}}, \forall j = 1, 2, \dots, L$  are eigenstates of  $\hat{H}_{\text{eff}}^{[2]}$  with eigenvalue  $\pm 2\Delta - 3/4\Delta$ . Similarly, one can construct two particle states, with particles placed on neighboring sites (on alternate rungs) in the following way,

$$\begin{aligned}
|j, 1\rangle_{2\text{P}} &= |\dots \overset{\circ}{\bullet}_j \overset{\circ}{\bullet}_{j+1} \dots\rangle \\
|j, 2\rangle_{2\text{P}} &= |\dots \overset{\bullet}{\circ}_j \overset{\bullet}{\circ}_{j+1} \dots\rangle
\end{aligned} \tag{S12}$$

which are zero modes of  $\hat{H}_{\text{eff}}^{[2]}$ ,  $\forall j = 1, 2, \dots, L$ . This construction can be generalized to many contiguous sites as follows,

$$\begin{aligned}
|j, 1\rangle_{3\text{P}} &= |\dots \overset{\circ}{\bullet}_j \overset{\circ}{\bullet}_{j+1} \overset{\circ}{\bullet}_{j+2} \dots\rangle \\
|j, 2\rangle_{3\text{P}} &= |\dots \overset{\bullet}{\circ}_j \overset{\bullet}{\circ}_{j+1} \overset{\bullet}{\circ}_{j+2} \dots\rangle
\end{aligned} \tag{S13}$$

Again the states,  $|j, 1\rangle_{3P}$  and  $|j, 2\rangle_{3P}$ ,  $\forall j = 1, 2, \dots, L$  are eigenvectors of  $\hat{H}_{\text{eff}}^{[2]}$  and the energy eigenvalue has to be determined by inspection. This procedure can be continued to yield more eigenvectors of  $\hat{H}_{\text{eff}}^{[2]}$ , until every other site in the ladder is filled, which leaves us with two eigenvectors  $|\mathbb{Z}_2\rangle$  and  $|\overline{\mathbb{Z}}_2\rangle$  which will be zero modes. Alternatively, one may also put non-contiguous excitations, which will again be exact eigenstates of the effective Hamiltonian

$$\begin{aligned} |(j_1, 1), (j_2, \pm)\rangle_{4P} &= \frac{1}{\sqrt{2}} \left( |\dots \circ \bullet \circ \bullet \dots \circ \bullet_{j_1} \dots \circ \bullet_{j_2} \dots\rangle \pm |\dots \bullet \circ \bullet \circ \dots \bullet_{j_1} \dots \bullet_{j_2} \dots\rangle \right) \\ |(j_1, 2), (j_2, \pm)\rangle_{4P} &= \frac{1}{\sqrt{2}} \left( |\dots \circ \bullet \circ \bullet \dots \bullet_{j_1} \dots \bullet_{j_2} \dots\rangle \pm |\dots \bullet \circ \bullet \circ \dots \circ_{j_1} \dots \circ_{j_2} \dots\rangle \right) \end{aligned} \quad (\text{S14})$$

with the condition that there is one insertion of  $|\circ\rangle$  between the block of spins at  $j_1, j_2$ . More non-zero modes of  $\hat{H}_{\text{eff}}^{[2]}$  can be constructed by placing ‘‘Bell-pair’’ like states which are separated by at least one insertion of  $|\circ\rangle$  in between. Following these simple rules one may enumerate all eigenvectors of  $\hat{H}_{\text{eff}}^{[2]}$ .

### B. Eigenvalues of $\hat{H}$ , $\hat{H}_{\text{eff}}^{[2]}$ and $\hat{H}_{\text{eff}}^{[4]}$

We note that although from an analytical point of view we do not have any understanding of  $\hat{H}_{\text{eff}}^{[4]} = \hat{H}_{\text{eff}}^{(0)} + \hat{H}_{\text{eff}}^{(2)} + \hat{H}_{\text{eff}}^{(4)}$ , or its eigenstates, we present below a comparison of the eigenvalues of the Hamiltonians  $\hat{H}$ ,  $\hat{H}_{\text{eff}}^{[2]}$  and  $\hat{H}_{\text{eff}}^{[4]}$ , where the construction and diagonalization of  $\hat{H}_{\text{eff}}^{[4]}$  was done using a numerical adaptation of Eq. (S7)

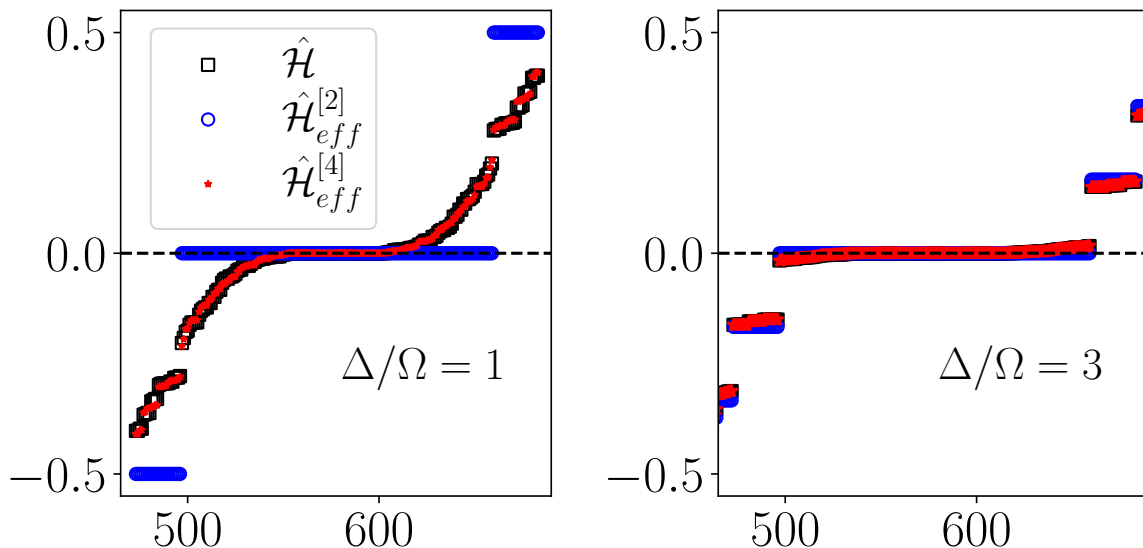


FIG. S2. Comparison of the spectrum of  $\hat{H}$  (black squares),  $\hat{H}_{\text{eff}}^{[2]}$  (blue circles) and  $\hat{H}_{\text{eff}}^{[4]}$  (red stars) [S6] for  $\Delta = 1$  (left panel) and  $\Delta = 3$  (right panel) with  $N = 16$  atoms (only the middle part of the spectrum is shown). This illustrates the fact that  $\hat{H}_{\text{eff}}^{[2]}$  can explain the lack of level repulsion for  $\Delta \sim 3$ , while for understanding the level repulsion nature of the exact spectrum at  $\Delta \sim 1$ , higher order processes (i.e. consideration of  $\hat{H}_{\text{eff}}^{[4]}$ ) become important.

### C. Ensemble of relaxation: Gibbs vs Generalized Gibbs

Under unitary quantum evolution via  $\hat{H}_{\text{eff}}^{[2]}$ , the system preserves the following operators:  $\hat{H}_{\text{eff}}^{[2]}$ ,  $\hat{Z}_\pi$  and  $\{\hat{Q}_j\}$ . This implies, that if the system evolves purely via  $\hat{H}_{\text{eff}}^{[2]}$ , at late times it should relax to the generalized Gibbs ensemble (GGE) described by appropriate Lagrange multipliers associated with these conservations laws (exact or approximate),

$$\hat{\rho}_{\text{GGE}} = \frac{1}{Z_{\text{GGE}}} \exp \left( -\beta \hat{H}_{\text{eff}}^{[2]} - \lambda_{\pi} \hat{Z}_{\pi} - \sum_{j=1}^L \lambda_j \hat{Q}_j \right) \quad (\text{S15})$$

where  $Z_{\text{GGE}}$  is a normalization factor which ensures that  $\text{Tr}(\hat{\rho}_{\text{GGE}}) = 1$ . On the other hand, as the additional extensive number of conservation laws are only approximate, the system (which evolves via  $\hat{H}$ ) should eventually relax (at timescales set by the fourth order effective Hamiltonian) to the Gibbs ensemble

$$\hat{\rho}_{\text{GE}} = \frac{1}{Z_{\text{GE}}} \exp \left( -\beta \hat{H} \right) \quad (\text{S16})$$

where  $Z_{\text{GE}}$  is a normalization constant such that  $\text{Tr}(\hat{\rho}_{\text{GE}}) = 1$ . For both cases, the relevant Lagrange multipliers i.e.  $\{\beta, \lambda_{\pi}, \lambda_{1,2,\dots,L}\}$  for GGE and  $\beta$  for GE, are determined by requiring the equality of the initial values of the conserved charges to the expectation values of conserved operators with respect to this ensemble. In practice, we have done this by minimizing the related cost functions  $f_{\text{GGE}}(\beta, \lambda_{\pi}, \lambda_1, \lambda_2, \dots, \lambda_L)$  and  $f_{\text{GE}}(\beta)$  using numerical optimization algorithms [S7]

$$f_{\text{GE}}(\beta) = \left( \text{Tr}(\hat{\rho}_{\text{GGE}} \hat{H}) - \text{Tr}(\hat{\rho}_0 \hat{H}) \right)^2 \quad (\text{S17})$$

$$f_{\text{GGE}}(\beta, \lambda_{\pi}, \lambda_1, \lambda_2, \dots, \lambda_L) = \sum_{\eta} \left[ \text{Tr}(\hat{\rho}_{\text{GGE}} \hat{K}_{\eta}) - \text{Tr}(\hat{\rho}_0 \hat{K}_{\eta}) \right]^2 \quad (\text{S18})$$

Where  $\{\hat{K}_{\eta}\}$  collectively stands for all the conserved quantities of  $\hat{H}_{\text{eff}}^{[2]}$ ,  $\hat{\rho}_0$  is the initial density operator and the dependence of  $\hat{\rho}_{\text{GE}}$  and  $\hat{\rho}_{\text{GGE}}$  on the Lagrange multipliers are implicitly assumed.

#### D. Storing classical bits of information

For  $\Delta \gg 1$ , utilizing the slow dynamics of the quasi-conserved charges  $\{\hat{Q}_j\}$ , it is possible to store  $L$  classical bits of information, in a square ladder with  $N = 2L$  sites, encoded via a class of appropriately chosen initial states labeled uniquely by the eigenvalues of  $\{\hat{Q}_j\}$ . This stored information can be retrieved at later times by performing simple projective readout measurements. To see how this can be achieved, consider a string of  $L$ -classical bits  $(c_1, c_2, \dots, c_L)$  where  $c_j \in \{-1, +1\}$ ,  $\forall j = 1, 2, \dots, L$ . Now, this classical string of bits can be encoded as initial values of the quasi-conserved local charges  $q_j$ 's at all rungs as  $q_j = c_j$ . As an example, in a ladder with  $N = 12$  sites, one can encode the classical information ‘‘bit-string’’  $(+1, +1, +1, -1, +1, -1, +1)$  in the initial quantum state  $|\psi(0)\rangle = |\circ\circ\bullet\circ\circ\circ\rangle$ . Although the eigenvalues of  $\{\hat{Q}_j\}$  are unique, the state  $|\psi\rangle$  is not and we can also start with the states  $|\circ\circ\bullet\circ\circ\circ\rangle, |\circ\circ\bullet\circ\bullet\circ\rangle, |\circ\circ\bullet\circ\circ\circ\rangle$  which also encode the same information. In the course of quantum dynamics via the full Hamiltonian  $\hat{H}$ , for  $\Delta \gg 1$ , the expectation values of all  $\hat{Q}_j$ 's stay almost frozen, and more importantly do not change their sign, for times as large as  $t \sim 10^4$ . This timescale is much beyond the times to which coherence can be maintained in experimental platforms [S8, S9]. By simple readout procedures, one can determine the sign of  $\langle \hat{Q}_j \rangle(t)$  at any time  $t$  during the quench experiment. By looking at this string of information, one can recover the encoded classical string  $(c_1, \dots, c_L)$  as

$$c_j = \frac{\langle \hat{Q}_j \rangle_t}{|\langle \hat{Q}_j \rangle(t)|} \quad \forall j = 1, 2, \dots, L \quad (\text{S19})$$

From the structure of Eq. (S8), it is easy to interpret the form of the initial Fock state required to encode the bit-string  $(c_1, \dots, c_L)$ .

#### S4. DERIVATION OF THE IDENTITY $\hat{C} e^{-i\hat{H}-\Delta_0\tau/2} \hat{C} = e^{+i\hat{H}+\Delta_0\tau/2}$

The identity  $\hat{C} e^{-i\hat{H}-\Delta_0\tau/2} \hat{C} = e^{+i\hat{H}+\Delta_0\tau/2}$  can be verified by expanding the exponential on its left hand side (LHS) in powers of  $\tau$  and showing that it is equal to the corresponding term in the right hand side (RHS). This equivalence for the  $m^{\text{th}}$  power is shown below

$$\begin{aligned}
& \hat{C} \frac{(-i\tau/2)^m}{m!} \overbrace{\left( \hat{H}_z + \hat{H}_x \right) \dots \left( \hat{H}_z + \hat{H}_x \right) \dots \left( \hat{H}_z + \hat{H}_x \right)}^{m \text{ terms}} \hat{C} \\
&= \frac{(-i\tau)^m}{2^m m!} \overbrace{\hat{C}^{-1} \left( \hat{H}_z + \hat{H}_x \right) \hat{C} \dots \hat{C}^{-1} \left( \hat{H}_z + \hat{H}_x \right) \hat{C} \dots \hat{C}^{-1} \left( \hat{H}_z + \hat{H}_x \right) \hat{C}}^{m \text{ terms}} \\
&= \frac{(-i\tau)^m}{2^m m!} \overbrace{\left( \hat{H}_z - \hat{H}_x \right) \dots \left( \hat{H}_z - \hat{H}_x \right) \dots \left( \hat{H}_z - \hat{H}_x \right)}^{m \text{ terms}} \\
&= \frac{(-i\tau)^m}{2^m m!} (-1)^m \overbrace{\left( -\hat{H}_z + \hat{H}_x \right) \dots \left( -\hat{H}_z + \hat{H}_x \right) \dots \left( -\hat{H}_z + \hat{H}_x \right)}^{m \text{ terms}} = \frac{(+i\tau)^m}{2^m m!} \hat{H}_{-\Delta_0}
\end{aligned} \tag{S20}$$

In the manipulations above, we have used the following two equations, which follow from the algebra of the Pauli spin- $\frac{1}{2}$  operators  $\{\hat{\sigma}^{x,y,z}\}$ .

$$\hat{C}^{-1} \hat{H}_z \hat{C} = +\hat{H}_z \tag{S21a}$$

$$\hat{C}^{-1} \hat{H}_x \hat{C} = -\hat{H}_x \tag{S21b}$$

### S5. STABILITY OF EXACT REVIVALS FOR AN IMPERFECT $\pi$ -PULSE

The exact revival protocols, namely Protocol-1 and Protocol-2 of the main text rely on the application of an exact many-body  $\pi$ -pulse. It is also important to know how stable these protocols are if one deviates from an exact  $\pi$ -pulse since small errors are likely in experimental scenarios. To this end we consider the modified version of the protocols, replacing the exact  $\pi$ -pulse with a  $\pi(1 - \epsilon)$  pulse. The modified protocols read

$$U_F^I(\tau, \epsilon) = \hat{T}_x e^{-i\pi(1-\epsilon)\hat{N}} e^{-i\hat{H}t} \tag{S22}$$

and

$$U_F^{II}(\tau, \epsilon) = e^{-i\pi(1-\epsilon)\hat{N}} e^{-i\hat{H}+\Delta_0 t} e^{-i\pi(1-\epsilon)\hat{N}} e^{-i\hat{H}-\Delta_0 t} \tag{S23}$$

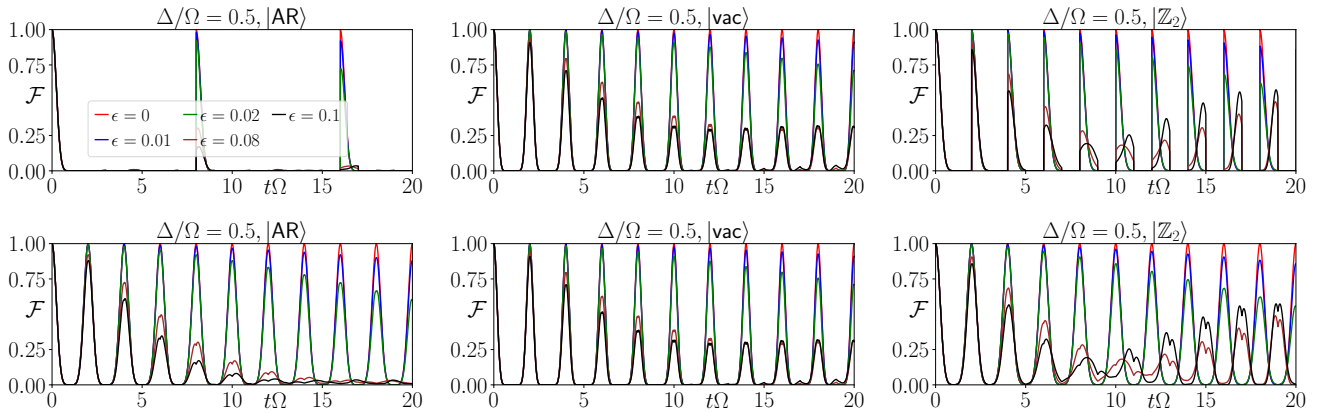


FIG. S3. Top: Stability of exact revivals under protocol (S22) starting from the states  $|AR\rangle$ ,  $|vac\rangle$  and  $|Z_2\rangle$ . Bottom: Same for protocol (S23)

## S6. 3-LEG LADDER

We now focus the 3-leg version of the model studied so far. Consider a 3-leg ladder with the same staggered detuning pattern along the longer direction of the lattice as before and the kinematic constrained shown in the main text. As before we consider periodic boundary conditions (PBC) along both directions, and the Hamiltonian now reads

$$\hat{H}_{3\text{-leg}} = \Omega \sum_{j=1}^L \sum_{a=1}^3 \hat{\sigma}_{j,a}^x - \Delta \sum_{j=1}^L \sum_{a=1}^3 (-1)^j \hat{\sigma}_{j,a}^z \quad (\text{S24})$$

where  $\hat{\sigma}_{j,a}^\alpha \equiv \hat{P}_{j+1,a}^\downarrow \hat{P}_{j-1,a}^\downarrow \hat{P}_{j,a-1}^\downarrow \hat{P}_{j,a+1}^\downarrow \hat{\sigma}_{j,a}^\alpha$  with  $\alpha = (x, y, z)$ . Henceforth we set  $\Omega = 1$  and comment on the nature of non-equilibrium dynamics of the 3-leg model for different regimes of  $\Delta$ . Fig. S4 illustrates the nature of the kinematic constraints.

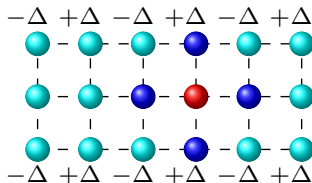


FIG. S4. Schematic of the 3-leg Rydberg ladder model: a spin-flip from take place from the spin-down to the spin-up state on a site (red) if only all of it's neighboring sites (blue) are in the spin-down state.

### A. Quantum many-body scars

We now consider quantum quench dynamics starting from simple initial product state (in Fock/computational basis). Due to the periodic boundary condition, it is not possible to accommodate the Néel state  $|\mathbb{Z}_2\rangle$  on a lattice with odd number of legs without violating the Rydberg blockading constraint. For this reason we do not consider the quantum quench dynamics at  $\Delta = 0$  in this case since for the 2-leg ladder it was the Néel state which showed anomalous revivals for this parameter choice. We shall instead focus on the dynamics from other initial states which are allowed in a 3-leg ladder configuration of the lattice such as  $|\text{vac}\rangle \equiv \left| \begin{smallmatrix} \circ\circ\circ\circ\circ\circ \\ \circ\circ\circ\circ\circ\circ \\ \circ\circ\circ\circ\circ\circ \end{smallmatrix} \right\rangle$  and the  $|1\text{P}\rangle \equiv \left| \begin{smallmatrix} \circ\circ\circ\circ\circ\circ \\ \circ\circ\bullet\circ\circ\circ \\ \circ\circ\circ\circ\circ\circ \end{smallmatrix} \right\rangle$  state at  $\Delta = 1$ .

As the left panel of Fig. S5 illustrates, for the case of the 3-leg ladder  $|\text{vac}\rangle$  shows anomalous revivals which the other state do not. Here for the  $|\text{vac}\rangle$  state one has  $\langle \text{vac} | \hat{H}_{3\text{-leg}} | \text{vac} \rangle = 0$  which, combined with the fact that the spectrum of (S24) has a spectral reflection symmetry implies that the system should relax to an infinite temperature ( $\beta_{\text{vac}} = 0$ ) GE. In contrast, for the  $|1\text{P}\rangle$  state, the initial energy density is  $\langle 1\text{P} | \hat{H}_{3\text{-leg}} | 1\text{P} \rangle = -2\Delta$ , which corresponds to a GE at inverse temperature  $\beta_{1\text{P}} \simeq -10^{-5}$ . However, our numerical results show that this state does not show any anomalous persistent revivals in the return probability (see Fig. S5 left panel).

### B. Quasi-conserved charges and Slow Dynamics for $\Delta \gg 1$

For  $\Delta \gg 1$ , the low-energy effective Hamiltonian can be obtained by in the same way as in Appendix-S3 by considering a 3-leg version of the generator for SW rotations (see Eq. (S4)). Similar to the 2-leg case, the effective low-energy Hamiltonian in this case (S25) only allows a specific spin-flip processes to take place if a “blockading” condition is satisfied. This specific blockading constraint and the spin-flip process can be understood in the same way as for the 2-leg case by considering the terms involving  $\hat{\sigma}^{x/y}$  in the second-order effective Hamiltonian which is given below (see Eq. S25). The PBC in both directions implies  $a - 2 \equiv a + 1$  and  $a + 2 \equiv a - 1$  for  $a = 1, 2, 3$ .

$$\begin{aligned} \hat{H}_{3\text{-leg,eff}}^{(2)} = & -\frac{1}{2\Delta} \sum_{j,a} (-1)^j \hat{\sigma}_{j,a}^z - \frac{1}{4\Delta} \sum_{j,a} \sum_{j',a'} (-1)^j \left[ \hat{P}_{j-1,a-1}^\downarrow \hat{P}_{j+1,a-1}^\downarrow \hat{P}_{j,a-2}^\downarrow \hat{P}_{j-1,a}^\downarrow \hat{P}_{j,a+1}^\downarrow \hat{P}_{j,a}^\downarrow (\hat{\sigma}_{j,a}^y \hat{\sigma}_{j,a-1}^y + \hat{\sigma}_{j,a}^x \hat{\sigma}_{j,a-1}^x) \right] \\ & + (-1)^j \left[ \hat{P}_{j-1,a+1}^\downarrow \hat{P}_{j+1,a+1}^\downarrow \hat{P}_{j-1,a}^\downarrow \hat{P}_{j+1,a}^\downarrow \hat{P}_{j,a-1}^\downarrow \hat{P}_{j,a+2}^\downarrow \hat{P}_{j,a}^\downarrow (\hat{\sigma}_{j,a}^y \hat{\sigma}_{j,a+1}^y + \hat{\sigma}_{j,a}^x \hat{\sigma}_{j,a+1}^x) \right] \end{aligned} \quad (\text{S25})$$

As a consequence, a class of initial states (specific Fock states) exhibit a simple motion that can be described by only considering the “blockaded-hopping” of the Rydberg excitations on the sites of the lattice allowed by  $\hat{H}_{3\text{-leg,eff}}^{[2]}$  for times before the effects of the fourth-order terms of the perturbative Hamiltonian sets in (see right panel of Fig. S5). For the initial state  $|1P\rangle \equiv \left| \begin{smallmatrix} \bullet & \circ & \circ & \circ & \circ & \circ \\ \circ & \circ & \circ & \circ & \circ & \circ \\ \circ & \circ & \circ & \circ & \circ & \circ \end{smallmatrix} \right\rangle$ , evolving under the action of  $\hat{H}_{3\text{-leg,eff}}^{[2]}$ , at any instant of time  $t$ , the quantum state can be written in the form  $|\psi(t)\rangle = \ell_1(t)|1,1\rangle + \ell_2(t)|1,3\rangle + \ell_3(t)|1,3\rangle$ , with  $|\ell_3(t)| = |\ell_2(t)|$  where  $|(j,a)\rangle$  denotes the one particle state with the particle/Rydberg excitation on the site  $(j,a)$  of the 3-leg ladder as indicated by the right panel of Fig. S5. The left panel of Fig. S5 illustrates the fidelity revivals for  $\Delta = 1$  starting from the vacuum and one-particle initial states.

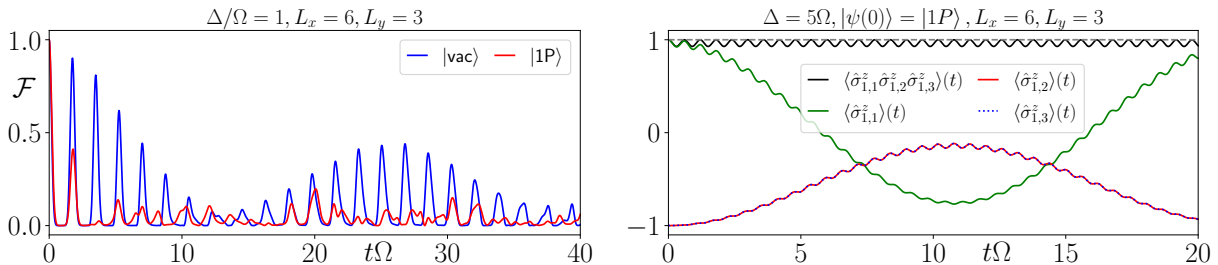


FIG. S5. Left: return probability  $\mathcal{F}(t) = |\langle \psi(0) | \psi(t) \rangle|^2$  starting from different initial states for  $\Delta = 1$  on a 3-leg ladder (see Eq. (S24)) with periodic boundary conditions. Right: illustration of 3-body conservation law  $\langle \hat{\sigma}_{1,1}^z \hat{\sigma}_{1,2}^z \hat{\sigma}_{1,3}^z \rangle$  (black solid curve) for the 3-leg ladder starting from a different one particle state i.e.  $|1P\rangle \equiv \left| \begin{smallmatrix} \bullet & \circ & \circ & \circ & \circ & \circ \\ \circ & \circ & \circ & \circ & \circ & \circ \\ \circ & \circ & \circ & \circ & \circ & \circ \end{smallmatrix} \right\rangle$ . In this case, the product of  $\hat{\sigma}^z$ 's on each rung behaves as an emergent conserved quantity

As a consequence of such a evolution, the 3-body operator  $\hat{\sigma}_{1,1}^z \hat{\sigma}_{1,2}^z \hat{\sigma}_{1,3}^z$  remains approximately conserved throughout the quantum evolution at  $\Delta = 5$ . This is qualitatively similar to the 2-leg square ladder case, where product of 2-body spin operators on the same rung remained approximately conserved. Thus, the results described in the main text for a 2-leg square ladder can be easily extended for a 3-leg square ladder with staggered detuning along the horizontal direction.

## S7. VAN DER WAALS INTERACTIONS AND VALIDITY OF THE FIRST NEAREST NEIGHBOR RYDBERG BLOCKADE

In a Rydberg atom quantum simulator setup (such as in [S8, S10]), neutral alkali atoms are trapped and arranged in a desired lattice geometry using the optical tweezer arrays, and are driven off-resonantly (with site-dependent detunings  $\Delta_{\vec{r}}$ ) with a laser that gives rise effective Rabi oscillations between the ground  $|G\rangle$  and the Rydberg excited state  $|R\rangle$  with frequency  $2\Omega$ . When the Rydberg excited states are  $|nS\rangle$ -type excited electronic orbitals, they interact dominantly via the van der Waals interaction and thus the Hamiltonian of the system reads

$$\hat{H}_{\text{Ryd}}^{\text{Full}} = \sum_{\vec{r}} (\Omega \hat{\sigma}_{\vec{r}}^x - \Delta_{\vec{r}} \hat{\sigma}_{\vec{r}}^z) + \frac{V_0}{2} \sum_{\vec{r}, \vec{r}'} \frac{\hat{n}_{\vec{r}} \hat{n}_{\vec{r}'}}{|\vec{r} - \vec{r}'|^6} \quad (\text{S26})$$

where  $\vec{r}$  denotes the position vectors of the trapped neutral atoms, which can be thought of as sites of a lattice. In Eq. (S26), the last double sum is taken over all possible pairs of atoms placed on sites  $\vec{r}, \vec{r}'$  of the ladder and  $\hat{n}_{\vec{r}} = (\hat{\sigma}_{\vec{r}}^z + 1)/2 = |R\rangle_{\vec{r}} \langle R|$  is the projection operator on the Rydberg excited state  $|R\rangle_{\vec{r}}$  at site  $\vec{r}$ .

To understand how accurately the idealized kinetically constrained model (Eq. (1) of the main text) mimics the features of the fully interacting long-range system Eq. (S26), we can make a direct comparison of the dynamics generated by these Hamiltonians. However, before considering the 2-leg case, we first we briefly revisit the 1D Rydberg chain and the associated 1D PXP model with the same goal. Finally we shall end this section with a brief discuss on the validity of Rydberg blockaded regime when the Rydberg atoms are arranged in a 2D square lattice in out-of-equilibrium scenarios.

### A. 1D Rydberg Chain

The Rydberg blockading regime can be realized from Eq. (S26), if the repulsive vdW interaction energy is much higher than other energy scales of the system. In such a scenario the system can be described by a simpler effective Hamiltonian obtained by perturbative analysis [S9]. In order to understand how accurately an effective Hamiltonian in a constrained Hilbert space represents the dynamics of the full system as depicted by Eq. (S26), we first focus on the paradigmatic PXP chain with site-dependent detunings  $\Delta_j$  (henceforth referred to as the PXP+Z model) and the fully interacting long-range model. The fully interacting long-range Hamiltonian for the 1D chain is the one dimensional analogue of Eq. (S26), and in the limit  $V_0 \gg \Delta_j, \Omega$  the low-energy effective Hamiltonian reads

$$\hat{H}_{\text{Ryd}}^{\text{eff}} = \sum_{j=1}^L \left( \Omega \hat{\sigma}_j^x - \Delta_j \hat{\sigma}_j^z \right) + \frac{V_0}{2} \sum_{|j-j'| > \text{NN}_1} \frac{\hat{n}_j \hat{n}_{j'}}{|j-j'|^6} \quad (\text{S27})$$

Here the double sum in Eq. (S27) is taken over all sites which are not nearest neighbors of each other. The interaction between the nearest neighbours are captured by the dressed spin-flip term  $\hat{\sigma}_j^x$  term. If the parameters  $V_0, \Omega, \Delta_j$  are such that  $V_0 \gg \Delta_j, \Omega \gg V_0/2^6$ , then the repulsive interaction term in (S27) is extremely small and the evolution of the system is entirely captured by the PXP+Z model. Such a situation is achieved by taking  $\Delta_j, \Omega \sim 1$  and  $V_0 = 10\Omega$ , in which case the condition  $V_0 \gg \Delta_j, \Omega \gg V_0/2^6$  is satisfied in an order of magnitude sense. If, however,  $V_0/2^6$  is not negligible compared to  $\Delta_j, \Omega$ , then the repulsive interaction term is going to play a significant role in the approximate evolution of the full system and needs to be considered. This is the case if, for example, the parameters are such that  $V_0 \gg \Delta_j, \Omega \gg V_0/3^6$  and we can only neglect long-range interactions at distances greater than two lattice separation units, in which case the Hamiltonian (S27) further simplifies to a short-range interacting Hamiltonian with the following form

$$\hat{H}_{\text{Ryd}}^{\text{eff, NN}_2} = \sum_{j=1}^L \left( \Omega \hat{\sigma}_j^x - \Delta_j \hat{\sigma}_j^z \right) + \frac{V_0}{2} \sum_{|j-j'| = \text{NN}_2} \frac{\hat{n}_j \hat{n}_{j'}}{|j-j'|^6} \quad (\text{S28})$$

Here  $|j-j'| = \text{NN}_2$  means that the double sum only contains the sites  $j, j'$  if they are separated by exactly two lattice separation units.

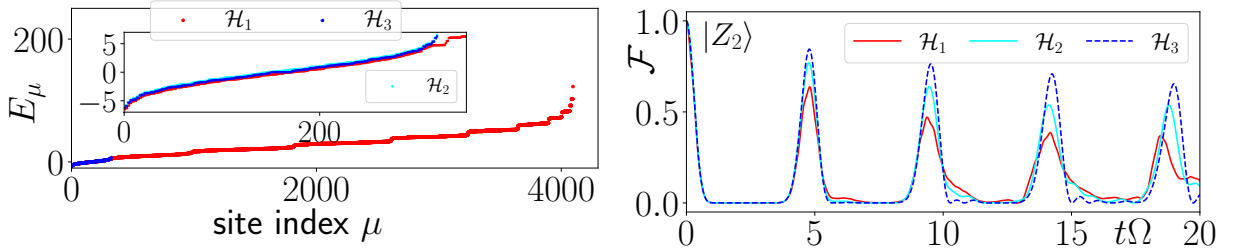


FIG. S6. 1D Rydberg chain as captured via the Hamiltonians (S26), (S28) and the PXP+Z model (denoted in the legend by  $\hat{H}_1$ ,  $\hat{H}_2$  and  $\hat{H}_3$  respectively) for  $N = 12$  atoms and  $V_0 = 10$ : (top panel) spectrum and (bottom panel) evolution of the return probability starting from the Néel state. See text for details.

In Fig. S6 we show a comparison of the eigenvalues of the Hamiltonians (S26),(S28): the left panel shows that the low-energy part of the spectrum of the full long-range interacting system (S26) can be faithfully captured by the entire spectrum of the kinetically constrained Hamiltonian (PXP+Z model). As the inset of this panel demonstrates, there is no qualitative difference in the energy eigenvalues even when the second nearest neighbor interactions (Eq. (S28)) are considered beyond the Rydberg blockade regime. The right panel Fig. S6 shows the evolution of the return probability starting from the Néel state and we can conclude that, although the qualitative features remain the same, there are quantitative differences in the behaviors predicted by Hamiltonians (S26), (S28) and the kinetically constrained model with no additional vdW interactions (which is the PXP+Z model in this case). Comparison of both spectral as well as dynamical features of these three descriptions indicate that the PXP+Z model provides a good qualitative description of the full long-range interacting many-body system described by Eq. (S26).

## B. 2-leg Rydberg Square Ladder

We now investigate the validity of the specific Rydberg blockade constraint for the 2-leg square ladder system, that was assumed throughout the main text, by considering the full long-range interacting system and its various approximations. The fully interacting long-range system is now given by the 2-leg square ladder version of Eq. (S26) while the low-energy effective Hamiltonian in the limit  $V_0 \gg \Delta_{j,a}, \Omega$  now reads

$$\hat{H}_{\text{Ryd}}^{\text{eff}} = \sum_{j=1}^L \sum_{a=1}^2 \left( \Omega \hat{\sigma}_{j,a}^x - \Delta_{j,a} \hat{\sigma}_{j,a}^z \right) + \frac{V_0}{2} \sum_{|\vec{r}-\vec{r}'| > \text{NN}_1} \frac{\hat{n}_{\vec{r}} \hat{n}_{\vec{r}'}}{|\vec{r}-\vec{r}'|^6} \quad (\text{S29})$$

It is crucial to note that the second nearest neighbor distance between two atoms in this case is the diagonal distance which is  $\sqrt{2}$  (in lattice separation units). This implies that for the 2-leg square ladder geometry, the conditions which the parameters  $V_0, \Delta_{j,a}, \Omega$  must satisfy so that the long-range interactions beyond the first neighbor could be neglected is  $V_0 \gg \Delta_{j,a}, \Omega \gg V_0/(\sqrt{2})^6$ . However, this condition cannot be met even in an order of magnitude sense, as can be seen, for example, by taking  $\Omega, \Delta_{j,a} \sim 1, V_0 = 10\Omega$  which is required to satisfy  $V_0 \gg \Delta_{j,a}, \Omega$ , but makes it impossible to satisfy  $\Delta_{j,a}, \Omega \gg V_0/(\sqrt{2})^6$ . This leads us to question if the specific form of the constraint assumed throughout the main text, is in practice realized in actual experiments in a Rydberg atom quantum simulator platform with  $nS$ -type orbitals.

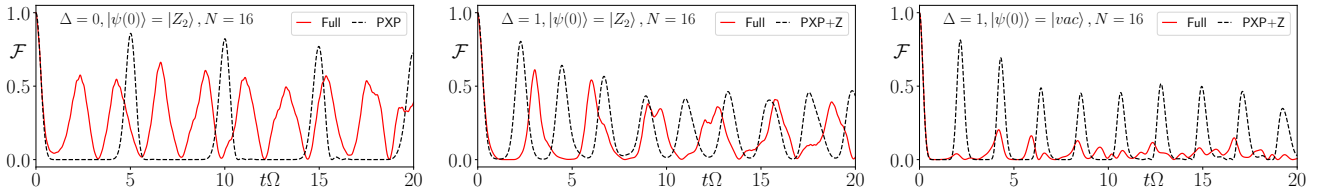


FIG. S7. Comparison of the return probability  $\mathcal{F} = |\langle \psi(0) | \psi(t) \rangle|^2$  by evolving an initial state under the fully interacting long-range Hamiltonian (S26) (red solid line) taking  $V_0 = 10$  and the idealized kinetically constrained system 2D PXP+Z model (black dashed lines) for  $N = 16$  atoms. The specific initial conditions are as follows: (top panel)  $|\psi(0)\rangle = |Z_2\rangle, \Delta = 0$  (middle panel)  $|\psi(0)\rangle = |Z_2\rangle, \Delta = 1$  and (bottom panel)  $|\psi(0)\rangle = |\text{vac}\rangle, \Delta = 1$ . In all cases the states have been evolved via exact diagonalization method.

To test this, in Fig. S7 (left panel) we compare the evolution of fidelity starting from the Néel state, under the fully interacting long-range Hamiltonian (S26), and the kinetically constrained Hamiltonian (Eq. (1) of main text). This figure shows that even the qualitative nature of quantum dynamics of these two Hamiltonians given by Eq. (S26) and Eq. (1) of main text are quite different from each other. This leads us to come to the conclusion that the kinetic constraint illustrated in Fig. (2) of the main text, is not a faithful representation of the actual long-range interacting system that would be realized in an experimental setup with  $nS$ -type excited electronic orbitals.

$$\hat{H}_{\text{Ryd}}^{\text{eff, NN}_2} = \sum_{j=1}^L \sum_{a=1}^2 \left( \Omega \hat{\sigma}_{j,a}^x - \Delta_{j,a} \hat{\sigma}_{j,a}^z \right) + \frac{V_0}{2} \sum_{\vec{r}, \vec{r}' \in \text{NN}_2} \frac{\hat{n}_{\vec{r}} \hat{n}_{\vec{r}'}}{|\vec{r}-\vec{r}'|^6} \quad (\text{S30})$$

From Fig. S7 (right panel) it is clear that the  $|\text{vac}\rangle$  state does not show any anomalous revivals when the full long-range interacting system is considered. However, as Figs. S7 left and middle panel demonstrate, the  $|Z_2\rangle$  state shows a substantial degree of anomalous revivals lasting several cycles, whose timescales cannot be explained from the PXP+Z approximation. However, these oscillations can be qualitatively described by augmenting the PXP+Z model with second nearest neighbor vdW interactions as in Eq. (S30). This conclusion is further supported by the fact that considering a short-range interacting system governed by the Hamiltonian of Eq. (S30), which is obtained from Eq. (S29) by considering interactions only up to the second-nearest neighbors, seems to capture both the spectral and dynamical features of the fully interacting long-range Hamiltonian (S26) (see Fig. S8)

In Fig. S8 the return probability  $\mathcal{F} = |\langle \psi(0) | \psi(t) \rangle|^2$  starting from the  $|Z_2\rangle$  state is shown as a function of time by evolving the state under the Hamiltonian (S26) (red solid line), (S30) (black dashed line) and (S31) (blue solid line) for a system with  $N = 12$  atoms at  $\Delta = 1$ . Thus for reasons mentioned above the second nearest-neighbor vdW interactions are essential in understanding the qualitative features of quantum dynamics depicted by the full long-range interacting system.

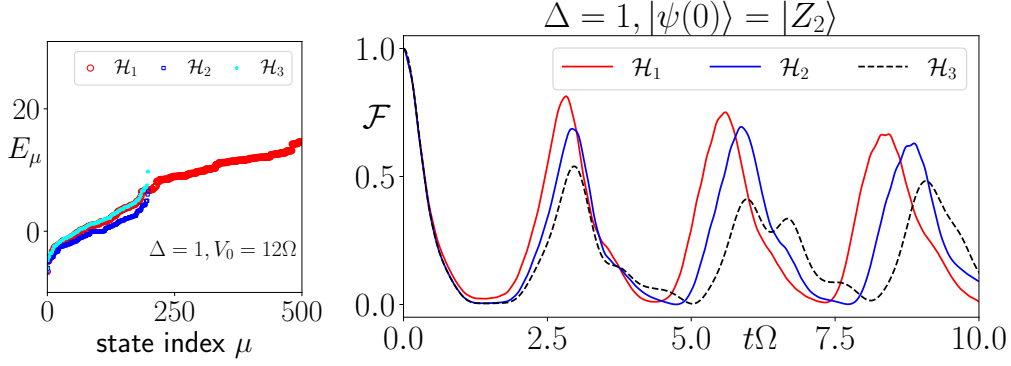


FIG. S8. *Left*: Comparison of the eigenvalues of the three Hamiltonians (S26),(S30) and (S31) (denoted by  $\hat{H}_1, \hat{H}_2$  and  $\hat{H}_3$  in the legend respectively) for  $\Delta = 1, V_0 = 12$ . Only the low-energy part of the spectrum has been displayed. *Right*: Comparison of the return probability  $\mathcal{F} = |\langle\psi(0)|\psi(t)\rangle|^2$  computed by evolving the initial state  $|\psi(0)\rangle = |Z_2\rangle$  state via three different Hamiltonians (S26),(S30),(S31) (denoted by  $\hat{H}_1, \hat{H}_3, \hat{H}_2$  in the legend respectively) for a system of  $N = 12$  atoms with  $\Delta = 1, V_0 = 12$  (see text for details) In all cases the state has been evolved by a discrete time-step integration method.

$$\hat{H}_{\text{Ryd}}^{\text{eff, NN}_2} = \sum_{j=1}^L \sum_{a=1}^2 (\Omega \hat{\sigma}_{j,a}^x - \Delta_{j,a} \hat{\sigma}_{j,a}^z) + \frac{V_0}{2} \sum_{\vec{r}, \vec{r}' \in \text{NN}_{1,2}} \frac{\hat{n}_{\vec{r}} \hat{n}_{\vec{r}'}}{|\vec{r} - \vec{r}'|^6} \quad (\text{S31})$$

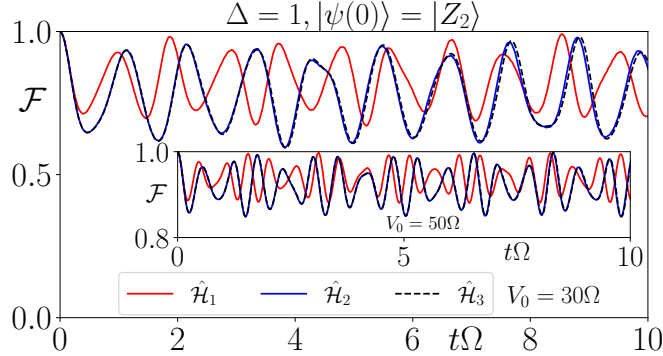


FIG. S9. Comparison of the return probability  $\mathcal{F} = |\langle\psi(0)|\psi(t)\rangle|^2$  computed by evolving the initial state  $|\psi(0)\rangle = |Z_2\rangle$  state via three different Hamiltonians (S26),(S30),(S31) (denoted by  $H_1, H_3, H_2$  in the legend respectively) for a system of  $N = 12$  atoms with  $\Delta = 1, V_0 = 30$  (main) and  $\Delta = 1, V_0 = 50$  (inset) respectively (see text for details) In all cases the state has been evolved by a discrete time-step integration scheme

It is also worth noting that increasing the strength of the vdW repulsive interaction (or equivalently reducing the lattice constant), increases the configurational energy of the Néel state (i.e.,  $\langle Z_2 | \hat{H}_{\text{Ryd}}^{\text{Full}} | Z_2 \rangle$ ) and results in confinement of this state (see Fig. S9). From the comparison between the dynamics obtained from the three different Hamiltonians Eqs. (S26), (S31), (S30), we can conclude that the confinement is a consequence of next nearest neighbor interaction, since the dynamics of the Néel state obtained by evolving the state via Hamiltonians (S30),(S31) agree qualitatively with that obtained from the fully interacting long-range system governed by (S26).

### C. Two Dimensional Square Lattice

The two dimensional (2D) PXP model has been shown to host QMBS [S11]. However, the inability of the kinetically constrained model such as Eq. (1) of the main text, to faithfully represent the quantum dynamics of the fully interacting long-range system (S26) for a 2-leg ladder geometry (see Appendix-S7), asks us to revisit the existence of QMBS in a physical two-dimensional Rydberg atom simulator in which vdW interactions are always present. The Hamiltonian for the 2D PXP+Z model (with site dependent detunings  $\Delta_{j,a} = (-1)^j \Delta$ ) of dimension  $L_x \times L_y$  is given by

$$\hat{H}_{\text{PXP}+\text{Z}}^{2\text{D}} = \Omega \sum_{j=1}^{L_x} \sum_{a=1}^{L_y} \hat{\sigma}_{j,a}^x - \Delta \sum_{j=1}^{L_x} \sum_{a=1}^{L_y} (-1)^j \hat{\sigma}_{j,a}^z, \quad (\text{S32})$$

where  $\hat{\sigma}_{j,a}^x \equiv \hat{P}_{j+1,a}^\downarrow \hat{P}_{j-1,a}^\downarrow \hat{P}_{j,a-1}^\downarrow \hat{P}_{j,a+1}^\downarrow \hat{\sigma}_{j,a}^x$

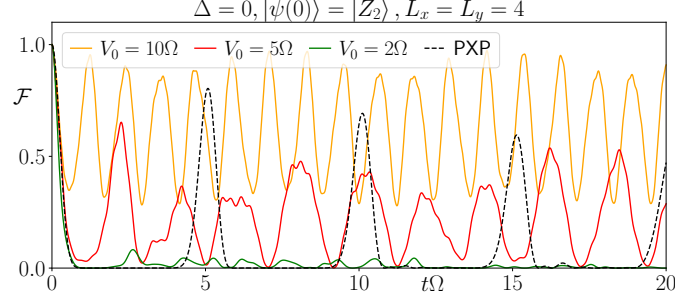


FIG. S10. Comparison of the return probability  $\mathcal{F} = |\langle \psi(0) | \psi(t) \rangle|^2$  as function of time  $t$  starting from the Néel state in the 2D geometry for a  $4 \times 4$  square lattice, computed with (i) full long-range interacting system (solid curves) with different vdW interaction strengths  $V_0 = 10$  (orange),  $V_0 = 5$  (red),  $V_0 = 2$  (green) and (ii) the idealized 2D PXP approximation (black dashed line) for  $\Delta = 0$  (see text for details). In all cases the states have been evolved via a discrete time-step integration scheme

Fig. S10 shows the comparison of the return probability of the initial Néel state ( $|\mathbb{Z}_2\rangle$ ) when evolved via the Hamiltonian Eq. (S32) (dashed black curve) with the corresponding results of the long-range interacting system for  $V_0 = 10$  (orange curve),  $V_0 = 5$  (red curve). The parameter choices  $V_0 = 10$  or  $V_0 = 5$  satisfies the condition  $V_0 \gg \Omega$  in a qualitative sense, however, the kinetically constrained model Hamiltonian does not capture the same dynamical behavior.

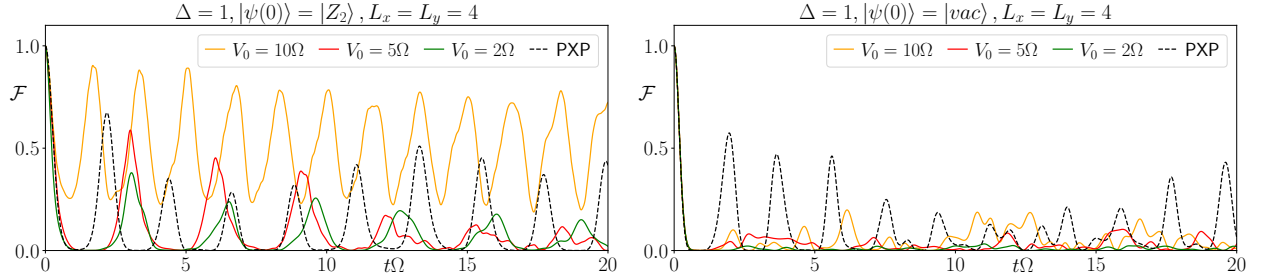


FIG. S11. Comparison of the return probability  $\mathcal{F} = |\langle \psi(0) | \psi(t) \rangle|^2$  as function of time  $t$  starting from (top panel) the Néel state  $|\mathbb{Z}_2\rangle$  and (bottom panel) the Rydberg vacuum state  $|\text{vac}\rangle$  in the 2D geometry for a  $4 \times 4$  square lattice, computed with (i) full long-range interacting system (solid curves) with different vdW interaction strengths  $V_0 = 10$  (orange),  $V_0 = 5$  (red),  $V_0 = 2$  (green) and (ii) the idealized 2D PXP approximation given by Eq. (S32) (black dashed line) for  $\Delta = 1$  (see text for details). In all cases the states have been evolved via a discrete time-step integration scheme.

We now turn on a non-zero staggered detuning ( $\Delta \neq 0$ ) and ask if the anomalous revivals from the  $|\mathbb{Z}_2\rangle$  and  $|\text{vac}\rangle$  state observed for the 2-leg square ladder geometry [S12], has any analogue in the 2D square lattice scenario.

From Fig. S11 we can see that in 2D the PXP+Z approximation given by Eq. (S32) does not fully capture the features of the full long-range interacting system accurately for  $V_0 = 2, 5, 10$ . The disagreement is more severe for the Rydberg vacuum initial state, as the PXP+Z predicts persistent oscillations lasting several cycles while the full long-range interacting system predicts this state does not have any noticeable revivals. This again leads us to conclude that for geometries in which the second nearest-neighbor distance is  $\sqrt{2}$  (in lattice separation units), the idealized strong Rydberg blockaded models do not faithfully capture the dynamics in these systems.

We end this section by noting that, realizing such geometric blockades, could in principle be made easier to achieve by leveraging anisotropic interactions as shown to exist for more complex Rydberg excited electronic states [S13]. However, such systems exhibit completely different kinds of effective spin interactions and the associated dynamics will exhibit vastly different phenomena.

## S8. SCALING OF THE NORM OF RESCALED, REGULARIZED ADIABATIC GAUGE POTENTIAL

The adiabatic gauge potential (AGP) is defined as the generator of adiabatic evolution of the eigenstates of the Hamiltonian, when some parameters of the Hamiltonian are varied. As in the rest of this paper, we are concerned with the behavior of the kinetically constrained model discussed in the main text, when  $\Omega = 1$ , and  $\Delta$  is varied, here we shall focus on the AGP  $\hat{\mathcal{A}}_\Delta$  defined as

$$\hat{\mathcal{A}}_\Delta |E_\mu(\Delta)\rangle = i\partial_\Delta |E_\mu(\Delta)\rangle \quad (\text{S33})$$

Where  $\hat{H}(\Delta) |E_\mu(\Delta)\rangle = E_\mu(\Delta) |E_\mu(\Delta)\rangle$  to understand whether the model given by Eq. (1) of the main text is chaotic for finite values of  $\Delta$  at times which are exponentially large in system size. The regularized AGP norm then reads [S14]

$$\|\hat{\mathcal{A}}_\Delta\|^2 = \frac{1}{\mathcal{D}_H} \sum_\nu \sum_{\mu \neq \nu} \frac{\omega_{\mu\nu}^2}{(\omega_{\mu\nu}^2 + \zeta^2)^2} |\langle E_\mu | \partial_\Delta \hat{H} | E_\nu \rangle|^2 \quad (\text{S34})$$

In the above equation, the sum on  $\mu, \nu$  runs over the Hilbert space (which may or may not be symmetry-reduced) and  $\zeta \propto N \log(N)$  is a cutoff introduced to regularize singularities arising due to degeneracies in the spectrum and  $\omega_{\mu\nu} \equiv E_\mu - E_\nu$ . Introducing this ultraviolet regulator  $\zeta$ , ensures that even if the symmetries of the Hamiltonian are not completely resolved, the regularized AGP norm gives a meaningful answer. In contrast almost all alternative measures of spectral statistics which are readily used as probes of the onset of quantum chaos (see Ref. [S15]), the knowledge and resolution of all symmetries of the Hamiltonian is essential. We note that the spectral form factor is an important exception, but necessarily relies on the introduction of disorder in the system to extract a clean signature for the onset of quantum chaos (the dip-ramp-plateau structure [S16]).

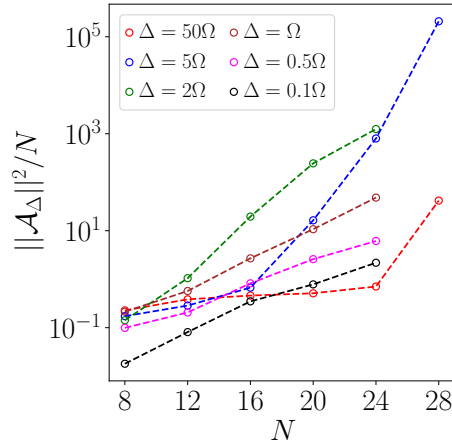


FIG. S12. Behavior of the rescaled, regularized AGP norm for a range of values of  $\Delta$  for system sizes  $N = 8, 12, 16, 20, 24, 28$ . In all cases  $\|\hat{\mathcal{A}}_\Delta\|^2/N$  increases in an exponential fashion as larger system sizes are accessed, which indicates that the 2-leg ladder Hamiltonian studied in the main text, is, as a whole, quantum chaotic, even if ergodicity breaking features of various forms exist for specific states and finite-size systems.

In Fig. S12 we show the rescaled norm of the regularized AGP i.e.  $\|\hat{\mathcal{A}}_\Delta\|^2/N$ , for a range of system sizes  $N = 8 - 28$ . This figure illustrates that  $\|\hat{\mathcal{A}}_\Delta\|^2/N$  grows with  $N$  in an exponential fashion for all regimes of  $\Delta$ . This exponential growth becomes noticeable only for larger system sizes when we are in the regime of emergent approximate conservation laws ( $\Delta \gg \Omega$ ) as seen by the data for  $\Delta = 5$  (blue open circles) and  $\Delta = 50$  (red open circles). In contrast for lower values of  $\Delta/\Omega$  such as  $\Delta = 2$  (green open circles),  $\Delta = 1$  (brown open circles),  $\Delta = 0.5$  (magenta open circles) and  $\Delta = 0.1$  (black open circles) the exponential growth seems noticeable even for small system sizes.

## S9. EFFECTS OF ENVIRONMENT

The relevant experimental platforms that host such model Hamiltonians, i.e., Rydberg atom quantum simulator platforms, have inevitable interactions with the environmental degrees of freedom [S17, S18]. The Rydberg excited

states have a finite lifetime and the Rydberg excited state of an atom undergoes spontaneous emissions, which projects it onto the Rydberg ground-state of that atom from time to time. For a single atom in such a platform, incoherent dynamics may appear as a result of fluctuations in the Rabi frequency and the detunings from one shot to another in a real experiment. These environmental effects at a single atom level can accumulate in an interacting many-body setup and give rise to interesting dynamics that cannot be explained by considering only unitary evolution governed by a Hamiltonian. Thus, it is important to check the robustness of the results obtained against such environmental loss channels. There are also other effects that may be present due to lattice imperfections and can be handled by considering a quenched disorder in the couplings of the Hamiltonian while still taking the system to be isolated and thus evolving unitarily.

In this section, we focus on studying the effect of the inevitable coupling to an external environment on the nature of the anomalous non-equilibrium dynamics discussed in the main text. In this paper we will only study the effects of two such environmental loss channels [S19]: (i) pure-dephasing and (ii) spontaneous emission of photons due to the finite lifetime of Rydberg excited states. Both of these effects have been addressed by considering the Lindblad master equation as a description of the quantum dynamics of this open quantum system. This Lindblad master equation is an equation of motion for the full density matrix of the system, which describes both coherent and dissipative parts of the evolution within the regime of Born-Markov approximation. The dissipative part of the quantum dynamics arising due to the aforementioned loss channels are manifested by the action of appropriate jump-operators  $\{\hat{J}_\alpha\}$  associated with the loss channels  $\{\alpha\}$ . For pure dephasing, these jump-operators take the form  $\hat{J}_{j,a}^{(d)} = \sqrt{\gamma_d} \hat{\sigma}_{j,a}^z$  while for spontaneous emission  $\hat{J}_{j,a}^{(e)} = \sqrt{\gamma_e} \hat{\sigma}_{j,a}^-$ , where  $\gamma_d$  and  $\gamma_e$  denote the strength of the dephasing and decay rate of the Rydberg excited-state respectively.

Within the Born-Markov approximation [S18], the full open quantum dynamics of a many-body quantum system (in terms of its density operator  $\hat{\rho}(t)$ ) is governed by the Gorini–Kossakowski–Sudarshan–Lindblad (GKSL) master equation, which is often referred to as simply the Lindblad master equation. This master equation has the following form

$$\begin{aligned} \frac{d\hat{\rho}(t)}{dt} &= \hat{\mathcal{L}}[\hat{\rho}(t)] \\ &= -i[\hat{H}, \hat{\rho}(t)] + \sum_{\alpha} \left( \hat{J}_{(\alpha)} \hat{\rho}(t) \hat{J}_{(\alpha)}^\dagger - \frac{1}{2} \left\{ \hat{J}_{(\alpha)}^\dagger \hat{J}_{(\alpha)}, \hat{\rho}(t) \right\} \right) \end{aligned} \quad (\text{S35})$$

Where  $\sum_{\alpha}$  symbolically denotes the sum over all quantum channels described by the jump operators  $\hat{J}_{(\alpha)}$ . In these subsequent sections, we will focus on (i) fate of the quantum many-body scar induced persistent oscillations observed in [S12] and (ii) robustness of the emergent approximate conservation laws (discussed in the main text) that appear in the limit ( $\Delta \gg 1$ ) when the two aforementioned environmental loss channels are considered.

## A. Stability of QMBS

### 1. Dephasing

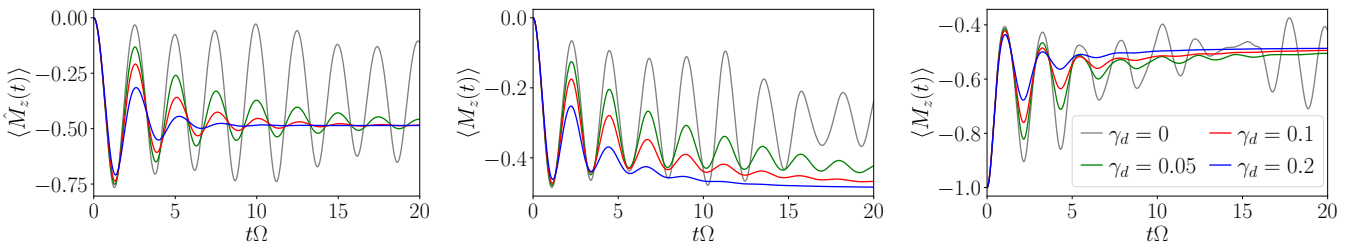


FIG. S13. Evolution of  $\langle \hat{M}_z(t) \rangle$  as a function of time  $t$  for (i)  $\Delta = 0, |\psi(0)\rangle = |\mathbb{Z}_2\rangle$ , (ii)  $\Delta = 1, |\psi(0)\rangle = |\mathbb{Z}_2\rangle$  and (iii)  $\Delta = 1, |\psi(0)\rangle = |\text{vac}\rangle$ , considering that the Rydberg atoms experience dephasing at a rate  $\gamma_d = 0, 0.05, 0.1, 0.2$

In Fig. S13, we show the evolution of average magnetization  $\langle \hat{M}_z(t) \rangle \equiv \text{Tr}[\hat{\rho}(t)\hat{M}_z]$ , where  $\hat{\rho}(t)$  is the instantaneous (normalized) density operator of the system governed by Eq. (S35) and  $\hat{M}_z \equiv \sum_{j=1}^L \sum_{a=1}^2 \hat{\sigma}_{j,a}^z / N$ . We consider three different combinations of the staggered detuning strength ( $\Delta$ ) and initial pure state ( $|\psi(0)\rangle$ ): (i)  $\Delta = 0, |\psi(0)\rangle = |\mathbb{Z}_2\rangle$ ,

(ii)  $\Delta = 1, |\psi(0)\rangle = |\mathbb{Z}_2\rangle$  and (iii)  $\Delta = 1, |\psi(0)\rangle = |\text{vac}\rangle$  in the presence of a non-zero dephasing  $\gamma_d$ . At these parameter points, the chosen states exhibit persistent oscillations due to presence of QMBS [S12] in the closed system undergoing unitary evolution. However, our results indicate that these persistent oscillations are not robust against dephasing: an increase in the dephasing rate diminishes the off-diagonal components of the density matrix (in Fock basis), resulting in the loss of coherent oscillations. In this steady-state ( $d\hat{\rho}/dt = 0$ ) all the Fock states have the same weight, which combined with the constrained nature of the Hilbert space of the system governed by Eq. (1) of main text implies that the steady-state magnetization value is close to  $-1/2$  in the presence of any non-zero dephasing, as evident from the Fig. S13. This figure also demonstrates that for very weak dephasing strengths e.g.,  $\gamma_d = 0.05$ , the persistent oscillations in average magnetization evolution do still appear in the same frequency of oscillation as observed for unitary evolution, albeit with a reduced amplitude.

## 2. Spontaneous emission

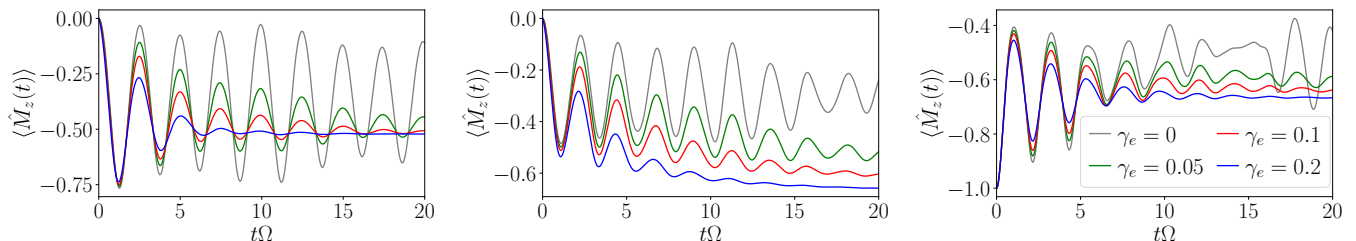


FIG. S14. Evolution of  $\langle \hat{M}_z(t) \rangle$  as a function of time  $t$  for (i)  $\Delta = 0, |\psi(0)\rangle = |\mathbb{Z}_2\rangle$ , (ii)  $\Delta = 1, |\psi(0)\rangle = |\mathbb{Z}_2\rangle$  and (iii)  $\Delta = 1, |\psi(0)\rangle = |\text{vac}\rangle$ , considering that the Rydberg excited state can spontaneously emit a photon with rate rate  $\gamma_e = 0$  (gray solid line),  $\gamma_e = 0.05$  (green solid line),  $\gamma_e = 0.1$  (red solid line), and  $\gamma_e = 0.2$  (blue solid line) respectively. See text for details.

In Fig. S14, we show the evolution of average magnetization  $\langle \hat{M}_z(t) \rangle$  as a function of time  $t$ , for (i)  $\Delta = 0, |\psi(0)\rangle = |\mathbb{Z}_2\rangle$ , (ii)  $\Delta = 1, |\psi(0)\rangle = |\mathbb{Z}_2\rangle$  and (iii)  $\Delta = 1, |\psi(0)\rangle = |\text{vac}\rangle$  considering that an atom in the Rydberg-excited state can spontaneously emit a photon at rate  $\gamma_e$  and relax to the Rydberg ground-state. As mentioned in the previous sections, for these parameter choices the isolated system ( $\gamma_e = 0$ ) exhibits persistent oscillations due to presence of QMBS (also see [S12]). For a non-zero spontaneous emission rate, there is a competition between the Rabi spin-flip term and the spontaneous emission term: if no spin-flip processes occur, then the system in the presence of spontaneous emissions, will continuously convert all the Rydberg-excited atoms into Rydberg ground-state atoms and the final steady-state will be the Rydberg vacuum state  $|\text{vac}\rangle$ . Thus, the steady-state expectation value of the average magnetization operator,  $\hat{M}_z$  would be  $-1$ , and  $\langle \hat{M}_z(t) \rangle$  would approach this value as time evolves, with the rate of approaching the steady-state being proportional to  $\gamma_e$ . When there are spin-flip processes induced by the Rabi oscillation term in the Hamiltonian, there will be competition between the strength of coherent oscillation in the constrained Hilbert space i.e. the Rabi frequency  $2\Omega$  and the strength of spontaneous emission  $\gamma_e$ . As a result, the steady-state magnetization value will depend on the specific choice of the parameter values used in the Lindblad evolution. For  $\Omega \gg \gamma_e$ , the steady-state magnetization ( $M_z^{\text{ss}}$ ) value would approach  $-1/2$ , i.e.,  $M_z^{\text{ss}} \sim -1/2$  (see top panel of Fig. S14) following the arguments given in Sec. S9 A 1, whereas in the opposite regime, i.e.,  $\Omega \ll \gamma_e$  one has  $M_z^{\text{ss}} \sim -1$ . In the intermediate regimes, the value of  $M_z^{\text{ss}}$  has to be computed explicitly by solving the equation of the steady-state  $d\hat{\rho}/dt = 0$ . In Fig. S14 we show the evolution of average magnetization  $\langle \hat{M}_z(t) \rangle$  as a function of time  $t$ , for the aforementioned three different combinations of  $\Delta, |\psi(0)\rangle$  at four representative values of the decay rate  $\gamma_e = 0$  (gray solid line),  $\gamma_e = 0.05$  (green solid line),  $\gamma_e = 0.1$  (red solid line), and  $\gamma_e = 0.2$  (blue solid line) respectively, for a ladder with  $N = 8$  atoms. The figures demonstrate that the persistent oscillations observed in the unitary evolution, are not robust against spontaneous emission for generic initial states. However, as observed in the bottom panel of Fig. S14, for the state  $|\psi(0)\rangle = |\text{vac}\rangle$ , consisting of all atoms in the Rydberg ground-state, the persistent oscillations in the magnetization dynamics are more robust against spontaneous emission.

## B. Stability of Approximate Emergent Conservation Laws

We now consider the behavior of the quasi-conserved charge  $\langle \hat{Q}_1(t) \rangle \equiv \text{Tr}[\hat{\rho}(t)\hat{Q}_1]$  under the time evolution governed by the Lindblad master equation (see Eq. (S35)). In Fig. S15 we consider three initial states, namely

(i)  $|\psi(0)\rangle = |Z_2\rangle$  (left panel), (ii)  $|\psi(0)\rangle = |1P\rangle$  (middle panel) and (iii)  $|\psi(0)\rangle = |\text{vac}\rangle$  (right panel) for a 2-leg ladder with  $N = 8$  atoms at  $\Delta = 4$  and different strengths of environmental loss channels:  $\gamma_d = 0.1$  (red solid curve),  $\gamma_d = 0.2$  (blue solid curve),  $\gamma_e = 0.1$  (red dashed curve),  $\gamma_e = 0.2$  (blue dashed curve),  $\gamma_d = \gamma_e = 0$  (gray solid curve). This figure exhibits the robustness of the conservation laws against the two aforementioned loss channels.

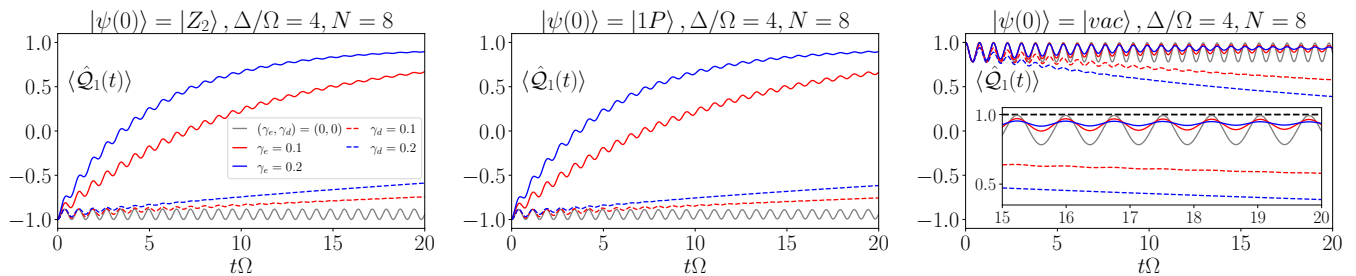


FIG. S15. Illustration of the stability of the emergent quasi-conserved charges  $\hat{Q}_1$  at  $\Delta = 4$  starting from three different initial states ( $|Z_2\rangle$  top panel,  $|1P\rangle$  middle panel and  $|\text{vac}\rangle$  bottom panel) under dephasing ( $\gamma_d \neq 0$ ) and spontaneous emission ( $\gamma_e \neq 0$ ) for a 2-leg ladder with  $N = 8$  atoms. Different colors in the figure indicate different values of the strength of the rate of dephasing and spontaneous emission with  $\gamma_e, \gamma_d = (0, 0)$  (gray solid line),  $\gamma_e = 0.1$  (red solid line),  $\gamma_e = 0.2$  (blue solid line),  $\gamma_d = 0.1$  (red dashed line) and  $\gamma_d = 0.2$  (blue dashed line) respectively. In all the figures, the colors are the same as that of the top panel. See text for details.

It is expected and also evident from Fig. S15 that for generic initial states, the emergent conservation laws are more stable against dephasing than compared to spontaneous emission, since one event of spontaneous emission of Rydberg-excited atoms on any of the sites  $(j, 1)$  or  $(j, 2)$  changes the sign of the quasi-conserved charge  $\hat{Q}_j$ . Furthermore, we note that pure dephasing does not alter the sign of the quasi-conserved charge  $\langle \hat{Q}_1(t) \rangle$  for all the initial states considered here up to times  $t \sim 20$ . Hence, the storage of  $L/2$  classical bits of information by the utilization of sign of such emergent approximate conservation laws as discussed in Appendix-S3D is a robust mechanism even in the presence of pure-dephasing. There is an important exception to this generic expectation: there exists one special initial state, namely the  $|\text{vac}\rangle$  state, for which the quasi-conserved charges seem to be more robust against spontaneous emission compared to dephasing. From the inset of the bottom panel of Fig. S15 it becomes evident that for the  $|\text{vac}\rangle$  state, an increased strength of the rate of spontaneous emission ( $\gamma_e$ ) enhances the degree of fulfillment of the approximate emergent conservation laws. This happens as after each event of spontaneous emission, one Rydberg excited-atom is converted into a Rydberg ground-state and hence the expectation value of the quasi-conserved charges shift towards the initial time expectation value with respect to the  $|\text{vac}\rangle$  state.

### C. Individual Quantum Trajectories

The evolution of the Lindblad master equation describes the non-unitary evolution of the system's density matrix within the Born-Markov approximation [S18]. This non-unitary nature of the dynamics arises from the fact that the system is interacting with the environment which results in incoherent evolution of the system's degrees of freedom. It is possible to describe the solution of the GKSL master equation as an average over the ensemble of density matrices constructed from several realizations of stochastically evolved pure quantum states where the stochasticity comes from the continuous monitoring of the quantum system under consideration. This completely equivalent approach known as Monte Carlo wave function (MCWF) approach, or as the quantum trajectory approach, allows one to track the evolution of the open system as a function of time in terms of pure quantum states [S18, S20–S23]. In the quantum trajectory approach, one evolves the quantum state  $|\psi(t)\rangle$ , which is a vector of dimension  $\mathcal{D}_H$  ( $\mathcal{D}_H$  being the Hilbert space dimension) and is thus computationally less expensive than the full Lindblad evolution. Apart from the lower numerical complexity, analysis of individual quantum trajectories are also important due to the fact that when a physical noisy quantum hardware under continuous monitoring evolves in time, it does not evolve according to the Lindblad evolution, but rather follows a stochastic pure state evolution which is similar to a single realization of a quantum trajectory, where the jumps  $\hat{J}_{(\alpha)}$  correspond to a manifestation of a physical loss in the system [S24]. The quantum trajectory approach also enables the possibility of monitoring quantum entanglement of the system under different continuous measurement processes [S25, S26].

As shown in Fig. S15, the emergent quasi-conserved charges, starting from a generic initial state, seem to be more

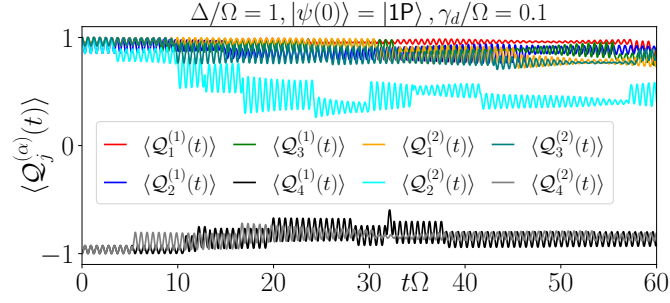


FIG. S16. Time evolution of the instantaneous expectation values of the approximate emergent conserved charges  $\hat{Q}_j^{(\alpha)}$  ( $j = 1, 2, 3, 4$  stands for rung index in a 2-leg square ladder with  $N = 8$  atoms) starting from the  $|1P\rangle \equiv |\circ\circ\circ\circ\circ\rangle$  state at  $\Delta = 5$ , for two different quantum trajectories  $\alpha = 1, 2$  when dephasing ( $\gamma_d = 0.1$ ) is considered. This figure shows that the sign of conserved charges do not alter during the evolution for two different realization of the quantum trajectory MCWF method. This is the case for most of the trajectories as the average Lindblad description also depicts the same scenario. See Fig. S15 and text for details.

robust against dephasing when compared to spontaneous emissions. For this reason, it is interesting to study individual quantum trajectories with dephasing as a loss channel. In Fig. S16, we show the evolution of all the quasi-conserved charges starting from the  $|1P\rangle$  state, when a dephasing rate  $\gamma_d = 0.1$  is considered. This figure illustrates that even for individual quantum trajectories, the conservation laws seem to be respected approximately. Moreover, the sign of the conserved charges do not change in time for a long duration, which further strengthens the classical bit storage capabilities illustrated in Appendix-S3D

- 
- [S1] A. W. Sandvik, Computational Studies of Quantum Spin Systems, *AIP Conf. Proc.* **1297**, 135 (2010), [arXiv:1101.3281 \[cond-mat.str-el\]](https://arxiv.org/abs/1101.3281).
- [S2] L. Amico, R. Fazio, A. Osterloh, and V. Vedral, Entanglement in many-body systems, *Rev. Mod. Phys.* **80**, 517 (2008).
- [S3] R. Islam, R. Ma, P. M. Preiss, M. Eric Tai, A. Lukin, M. Rispoli, and M. Greiner, Measuring entanglement entropy in a quantum many-body system, *Nature* **528**, 77 (2015).
- [S4] B. Groisman, S. Popescu, and A. Winter, Quantum, classical, and total amount of correlations in a quantum state, *Phys. Rev. A* **72**, 032317 (2005).
- [S5] F. Verstraete, M. Popp, and J. I. Cirac, Entanglement versus correlations in spin systems, *Phys. Rev. Lett.* **92**, 027901 (2004).
- [S6] We have computed the fourth-order effective Hamiltonian  $\hat{\mathcal{H}}_{\text{eff}}^{[4]}$  numerically by constructing the generator  $i\hat{\mathcal{S}}$  in the computational basis and explicitly performing the rotation upto desired order in perturbation theory. In practice this could be continued to any order desired, however, such a numerical construction of higher-order effective Hamiltonians does not offer any insights into the physical process the system exhibits, which closed analytical expressions can offer.
- [S7] P. Virtanen, R. Gommers, T. E. Oliphant, M. Haberland, T. Reddy, D. Cournapeau, E. Burovski, P. Peterson, W. Weckesser, J. Bright, S. J. van der Walt, M. Brett, J. Wilson, K. J. Millman, N. Mayorov, A. R. J. Nelson, E. Jones, R. Kern, E. Larson, C. J. Carey, Í. Polat, Y. Feng, E. W. Moore, J. VanderPlas, D. Laxalde, J. Perktold, R. Cimrman, I. Henriksen, E. A. Quintero, C. R. Harris, A. M. Archibald, A. H. Ribeiro, F. Pedregosa, P. van Mulbregt, and SciPy 1.0 Contributors, SciPy 1.0: Fundamental Algorithms for Scientific Computing in Python, *Nature Methods* **17**, 261 (2020).
- [S8] H. Bernien, S. Schwartz, A. Keesling, H. Levine, A. Omran, H. Pichler, S. Choi, A. S. Zibrov, M. Endres, M. Greiner, V. Vuletić, and M. D. Lukin, Probing many-body dynamics on a 51-atom quantum simulator, *Nature* **551**, 579 (2017).
- [S9] D. Bluvstein, A. Omran, H. Levine, A. Keesling, G. Semeghini, S. Ebadi, T. T. Wang, A. A. Michailidis, N. Maskara, W. W. Ho, S. Choi, M. Serbyn, M. Greiner, V. Vuletić, and M. D. Lukin, Controlling quantum many-body dynamics in driven rydberg atom arrays, *Science* **371**, 1355 (2021), <https://www.science.org/doi/pdf/10.1126/science.abg2530>.
- [S10] D. Bluvstein, H. Levine, G. Semeghini, T. T. Wang, S. Ebadi, M. Kalinowski, A. Keesling, N. Maskara, H. Pichler, M. Greiner, V. Vuletić, and M. D. Lukin, A quantum processor based on coherent transport of entangled atom arrays, *Nature* **604**, 451 (2022).
- [S11] C.-J. Lin, V. Calvera, and T. H. Hsieh, Quantum many-body scar states in two-dimensional rydberg atom arrays, *Phys. Rev. B* **101**, 220304 (2020).
- [S12] M. Pal, M. Sarkar, K. Sengupta, and A. Sen, Scar-induced imbalance in staggered rydberg ladders, *Phys. Rev. B* **111**, L161101 (2025).
- [S13] B. Vermersch, A. W. Glaetzle, and P. Zoller, Magic distances in the blockade mechanism of rydberg  $p$  and  $d$  states, *Phys. Rev. A* **91**, 023411 (2015).

- [S14] M. Pandey, P. W. Claeys, D. K. Campbell, A. Polkovnikov, and D. Sels, Adiabatic eigenstate deformations as a sensitive probe for quantum chaos, *Phys. Rev. X* **10**, 041017 (2020).
- [S15] L. F. Santos and M. Rigol, Onset of quantum chaos in one-dimensional bosonic and fermionic systems and its relation to thermalization, *Phys. Rev. E* **81**, 036206 (2010).
- [S16] L. D'Alessio, Y. Kafri, A. Polkovnikov, and M. R. and, From quantum chaos and eigenstate thermalization to statistical mechanics and thermodynamics, *Advances in Physics* **65**, 239 (2016), <https://doi.org/10.1080/00018732.2016.1198134>.
- [S17] H. Weimer, M. Müller, I. Lesanovsky, P. Zoller, and H. P. Büchler, A rydberg quantum simulator, *Nature Physics* **6**, 382 (2010).
- [S18] A. J. Daley, Quantum trajectories and open many-body quantum systems, *Advances in Physics* **63**, 77–149 (2014).
- [S19] H. Tamura, T. Yamakoshi, and K. Nakagawa, Analysis of coherent dynamics of a rydberg-atom quantum simulator, *Phys. Rev. A* **101**, 043421 (2020).
- [S20] P. Zoller, M. Marte, and D. F. Walls, Quantum jumps in atomic systems, *Phys. Rev. A* **35**, 198 (1987).
- [S21] P. Zoller, Monte carlo simulation of the quantum master equation for vacuum, thermal, and squeezed reservoirs, in *Optical Society of America Annual Meeting* (Optica Publishing Group, 1992) p. MFF2.
- [S22] R. Dum, P. Zoller, and H. Ritsch, Monte carlo simulation of the atomic master equation for spontaneous emission, *Phys. Rev. A* **45**, 4879 (1992).
- [S23] K. Mølmer, Y. Castin, and J. Dalibard, Monte carlo wave-function method in quantum optics, *J. Opt. Soc. Am. B* **10**, 524 (1993).
- [S24] A. J. Daley, J. M. Taylor, S. Diehl, M. Baranov, and P. Zoller, Atomic three-body loss as a dynamical three-body interaction, *Phys. Rev. Lett.* **102**, 040402 (2009).
- [S25] T. Vovk and H. Pichler, Entanglement-optimal trajectories of many-body quantum markov processes, *Phys. Rev. Lett.* **128**, 243601 (2022).
- [S26] T. Vovk and H. Pichler, Quantum trajectory entanglement in various unravelings of markovian dynamics, *Phys. Rev. A* **110**, 012207 (2024).